Aalborg Universitet

Reconstruction Algorithms in Undersampled AFM Imaging

Arildsen, Thomas; Oxvig, Christian Schou; Pedersen, Patrick Steffen; Østergaard, Jan; Larsen, Torben

Reconstruction Algorithms in Undersampled AFM Imaging

Thomas Arildsen, *Member, IEEE,* Christian Schou Oxvig, *Student Member, IEEE,* Patrick Steffen Pedersen, *Member, IEEE,* Jan Østergaard, *Senior Member, IEEE,* and Torben Larsen, *Senior Member, IEEE,*

Abstract—This paper provides a study of spatial undersampling in atomic force microscopy (AFM) imaging followed by different image reconstruction techniques based on sparse approximation as well as interpolation. The main reasons for using undersampling is that it reduces the path length and thereby the scanning time as well as the amount of interaction between the AFM probe and the specimen. It can easily be applied on conventional AFM hardware. Due to undersampling, it is necessary to subsequently process the acquired image in order to reconstruct an approximation of the image. Based on real AFM cell images, our simulations reveal that using a simple raster scanning pattern in combination with conventional image interpolation performs very well. Moreover, this combination enables a reduction by a factor 10 of the scanning time while retaining an average reconstruction quality around $36\,\mathrm{dB}$ **PSNR** on the tested cell images.

Index Terms—atomic force microscopy, undersampling, image reconstruction, sparse approximation, interpolation, compressed sensing

I. INTRODUCTION

ATOMIC force microscopy (AFM) is a scanning probe microscopy technique that offers several interesting possibilities in the imaging of biological materials such as cells. Atomic force microscopy complements other microscopy techniques such as optical microscopy or scanning electron microscopy (SEM) by enabling three-dimensional imaging of cell surfaces and imaging cells and bio-molecules in more natural environments than other techniques. This also enables imaging of live cells [1]. Imaging biological material such as live cells does, however, entail some challenges such as the risk of damaging the cells due to interaction with the microscope probe tip [2], [3].

Imaging with AFM equipment is a relatively time-consuming process, taking on the order of seconds to minutes or even higher to image a region of interest using commercial AFM equipment [4], [5]. While this may be inconvenient to the operator of AFM equipment, it can become an impediment when imaging temporally evolving material and organisms, i.e. the AFM equipment may simply not be able to scan the specimen sufficiently fast to be able to follow the process [6], [7]. Several approaches to achieving higher-speed scanning in AFM have been explored. These include approaches dealing with the mechanical characteristics of the equipment, control of the probe, or design of special sampling patterns that allow faster movement of the probe [6], [8]–[10]. However, since it is often necessary to probe the specimen with great caution, particularly in the case of live cell imaging, efforts to scan faster and yet interact as little/carefully with the specimen as possible may well run counter to each other.

One way to combat this dilemma could be to use sparser sampling patterns than the patterns typically used in AFM. The typical way to sample the topography of a specimen in AFM is to scan the probe across the surface in a dense raster pattern [11]. This process can be sped up by using a sparser sampling pattern, i.e. effectively letting the scan path cover the surface less densely and thereby enabling a shorter and thus faster scan path. This approach simultaneously causes the probe tip to interact less with the specimen. Such an approach can potentially solve the dilemma of careful interaction with a fragile specimen vs. fast scanning. In exchange, this necessitates reconstruction of the full surface topography (image) from considerably fewer samples instead.

In this paper we survey a range of methods that can be applied in order to achieve faster and/or less destructive cell imaging using AFM.[1] In particular, we compare two different sampling patterns (raster and spiral) in combination with a selection of image reconstruction techniques based on sparse approximation and an interpolation technique used as reference. For the comparison, we use seven AFM cell image specimens. We identify useful combinations of scanning patterns and reconstruction algorithms that provide good reconstruction quality and are sufficiently fast w.r.t. scan time as well as reconstruction time. A perhaps somewhat surprising finding is that the naive approach of simply scanning the cell specimen with a less dense raster pattern, effectively skipping a fraction of the lines, and then combined with standard image interpolation, leads to the best overall objective reconstruction quality for a fixed undersampling ratio. It is worth noticing that if obtaining a less dense raster scanning pattern is supported by the AFM equipment, then this technique does not require

[1] The underlying code-base and images required for reproducing all results in this article is freely available at:
- **Code** http://dx.doi.org/10.5281/zenodo.32959
- **Results** http://dx.doi.org/10.5281/zenodo.32958
- **Images** http://dx.doi.org/10.5281/zenodo.17573

any hardware modification of the AFM equipment. The reconstruction algorithm is then a purely software-based approach that can be performed on a standard PC or enabled through a firmware upgrade of the equipment. We also find that for the seven AFM cell images considered in this study, interpolation and total variation techniques work better with raster scanning patterns, whereas sparse approximation techniques with DCT dictionaries work better with spiral scanning patterns.

The paper is outlined as follows. In Section II we give an overview of signal processing for atomic force microscopy, introducing the basics of AFM equipment as well as the necessary processing required to obtain useful images from the equipment, possible impairments, and notation details. In Section III we give an overview of image reconstruction based on sparse approximation techniques and introduce a reference method, interpolation, for comparison. Section IV details our experiments regarding reconstruction of images in AFM. Section V presents results from numerical experiments with the presented reconstruction methods. Finally, Section VI summarizes and concludes the paper.

II. NOTATION AND FRAMEWORK

A. Introduction to AFM

Atomic force microscopy (AFM) is one of the most advanced techniques for investigating and manipulating surfaces on the atomic scale. By working on this scale, AFM provides magnification which is orders of magnitude beyond the capabilities of optical, confocal, and even scanning electron microscopy or transmission electron microscopy techniques [12]. This is generally the case for scanning probe microscopy (SPM) which encompasses the families of AFM and scanning tunneling microscopy (STM). Whereas STM requires the surface of interest to be electrically conductive, AFM does not [11] and is therefore the technique of interest to the present paper due to the potential application to live cell imaging. However, many of the thoughts presented should be applicable to SPM in general.

Being a state-of-the-art technique, AFM is used extensively within nanoscale science and technology [13]. Partly because the technique can be used on surfaces in both vacuum, air, and liquids, there is a large variability in the applications [7]. A number of applications relate to materials science, some to the study of biological processes, and some to the study of biological materials [9]. Yet other applications use AFM for surface manipulation including lithography, nanomanipulation, and nanoassembly [14].

In the context of surface investigation, AFM is most commonly used to generate a 3D surface map of the object of interest [6]. Loosely speaking, a probe is used to measure the height of the surface while the probe and the surface are moved relative to each other. Specifically, the vertical position of the probe is controlled by a piezo which is itself controlled by a feedback loop. This feedback loop keeps a particular measured property constant, such as the deflection of the cantilever on which the probe tip is located, in order to ensure that the probe traces the surface. Independently of this control loop, the probe and the surface are moved relative to each other by the use of additional piezos [12].

B. Image acquisition

To prepare the AFM equipment for operation, the user must perform an initial system setup which consists of a number of steps. Some of these steps require the user to make decisions based on the surface under investigation. These decisions include selecting a cantilever, operating mode (contact mode, acoustic AC mode, or magnetic AC mode), servo settings or AC mode settings, and scanner settings. Although these heavily affect the quality of the measurements of the surface, an in-depth coverage of the initial system setup is beyond the scope of the present paper. It is, however, worth mentioning that the degree of interaction between the probe tip and sample depends heavily on the chosen operating mode. In contact mode, the probe tip is "dragged" across the surface and thus typically applies a near-constant force to it [12]. In AC mode on the other hand, the cantilever is oscillated and thus only applies force to the surface a fraction of the time [15]. The interaction between probe tip and sample is particularly important when dealing with soft materials such as biological cells [16].

The setup of the AFM equipment includes a number of steps related to the movement of the probe and the surface relative to each other: i.e. the scanning path. Traditionally, a raster scanning path is used [4], and this only requires the user to decide which surface region to scan, how densely to scan it, and how fast to scan it. If the raster scanning path should not be used then the user is required to decide on the actual scanning path, the movement speed of the probe, and the sampling frequency. Additionally, when deciding on a non-raster scanning path, the user is required to somehow implement this scanning if it is not already available in the AFM equipment.

The actual scanning path is subject to two major constraints: 1) The probe cannot easily or effectively "jump" from one point on the surface to another. Therefore, the path must be continuous. 2) The piezos have a band limited frequency response. Therefore, when combined with a specific probe movement speed, the path must have frequency contents which are limited to that band in order to avoid distorting the scanning path.

C. Acquisition impairments

The image acquisition process is subject to a number of impairments. Some of these impairments may severely affect the image quality when image reconstruction is introduced [17]. To ensure successful image reconstruction, the impairments must be considered. Fortunately, some of these can be mitigated by careful setup of the AFM equipment whereas others must be accounted for in the image reconstruction [11]. This section highlights some of the possible impairments but should in no way be considered a complete list.

Some of the impairments relate to the object of interest. First of all, when this object is put in place, the surface is likely to be tilted since the user cannot likely ensure that the surface is perfectly normal to the probe tip. This impairment should be accounted for by the image reconstruction. Next, when acquiring an image, the surface may be deformed [18] since

the AFM equipment applies force to the object which may consist of a soft material. This impairment can be mitigated by careful setup of the AFM equipment but it inevitably distorts the image slightly [6].

Some of the impairments relate to the physical parts of the AFM equipment. The probe tip is affected by an area of the surface rather than a single point because of the shape and size of the probe [11]. Depending on the probe, the slope of the surface, and the desired physical resolution, this may distort the image slightly. The sensors used in state-of-the-art AFM equipment are sufficiently accurate and precise to only cause negligible impairments [9]. The piezos used to move the sample and probe relative to each other are intrinsically subject to non-linearity, hysteresis, and creep [14]. However, state-of-the-art AFM equipment can operate in closed-loop mode in order to mitigate these effects [8].

Some of the impairments relate to the control loops and the applied signal processing. The probe is part of a cantilever which is deflected when the probe tip is affected by the sample surface. This deflection is measured and compared to the desired deflection resulting in an error signal which is used to control the piezo. However, due to the filters used, the type of controller, and the physics of piezos, the piezo does not instantaneously compensate for changes in cantilever deflection which may distort the image [18]. This impairment may be mitigated by reducing the probe movement speed.

Finally, there are also possible issues of stochastic measurement noise. Several factors specific to the equipment contribute to stochastic noise in AFM [19]. These are for example related to the optical system that is used to control the deflection of the cantilever.

D. Discretization

As described in Section II-A, imaging with AFM can be seen as measuring the surface height of a specimen across a continuous two-dimensional surface (topography). The end goal we consider here is conveying this measured topography visually. This typically entails displaying an image of the measured surface as points on a uniform grid, e.g. a computer screen. This can be done in various ways, some of which are described in the following. In order to do that, we first establish some notation and general principles here.

We consider a region $\Omega \subset \mathbb{R}^2$ within which we wish to image the topography of the continuous surface of the specimen, denoted X. The surface of the specimen is sampled along a scan path, on which the AFM probe, represented by the sampling operator ϕ, collects m samples $\phi(X) \in \mathbb{R}^{m \times 1}$ at discrete points on the surface X. From these samples, we wish to reconstruct an $h \times w$ (pixels) image of the surface. We refer to this image representation of the surface (with values located on a uniform pixel grid over Ω) as a matrix, $\mathbf{X} \in \mathbb{R}^{h \times w}$, or as a vector, $\mathbf{x} \in \mathbb{R}^{hw \times 1}$, containing the stacked columns of the matrix with the left-most column of $\mathbf{X}$ as the top entries of $\mathbf{x}$ etc. The reconstruction of this image is correspondingly denoted $\hat{\mathbf{X}}$ or $\hat{\mathbf{x}}$.

In the case of raster scanning as traditionally applied in AFM, the sampled points can be chosen naturally to lie close to a uniform grid that fits directly into an image interpretation. In this case the sampled points $\phi(X)$ correspond directly to the image $\mathbf{X}$ with the possible addition of noise and various scanning artifacts $\mathbf{E} \in \mathbb{R}^{h \times w}$ as described in Section II-C:

$$\phi(X) = \mathbf{X} + \mathbf{E} \tag{1}$$

If one deviates from this traditional raster scanning and sampling approach by either changing the scan pattern or using non-uniform sampling, the acquired image samples do not generally fall on a uniformly spaced grid corresponding to the pixels of $\mathbf{X}$. Having a uniformly spaced pixel grid is attractive from a mathematical point of view, since the image can be represented in a matrix form with an intuitive interpretation of the physical locations of the sampling points. In this case, we consider reconstruction $\hat{\mathbf{X}}$ of the hypothetical image $\mathbf{X}$ from which measurements are obtained via an intermediate interpolation from the measured points to the pixel grid. In this spatially discretized setting, the obtained samples can be seen as located at points on the uniform pixel grid as well such that:

$$\phi(X) = \mathbf{\Phi}\mathbf{x} \tag{2}$$

The pattern of sampling points represented by the spatially discrete matrix $\mathbf{\Phi}$ is referred to as the sampling pattern.

The variables defined in this section form the basis of the different reconstruction approaches presented in the following sections.

III. SPARSE APPROXIMATION

Sparse regularization and/or approximation is a well-known approach to solving ill-posed optimization problems, early examples of which include [20]–[22]. The principle of compressed sensing which has emerged quite recently has popularized the sparse regularization principle [23], [24]. For an introduction, see [25]–[27].

In this paper, we demonstrate a selection of reconstruction algorithms based on sparse regularization. For this purpose, we consider the following linear measurement model:

$$\mathbf{y} = \mathbf{A}\boldsymbol{\alpha} \tag{3}$$

The vector $\boldsymbol{\alpha} \in \mathbb{R}^{n \times 1}$ is a sparse vector, i.e. it contains only $k \ll n$ non-zero entries, also expressed as $\|\boldsymbol{\alpha}\|_0 = k$ in the ℓ_0 pseudo-norm. The matrix $\mathbf{A} \in \mathbb{R}^{m \times n}$ is a sensing matrix applied to the sparse vector to sample the measurements $\mathbf{y} \in \mathbb{R}^{m \times 1}$.

Typically, as is the case for the application to AFM proposed here, a signal is not sparse in the domain we can observe it in. The following more general model is therefore used:

$$\mathbf{y} = \mathbf{\Phi}\mathbf{x} \tag{4}$$

where:

$$\mathbf{x} = \mathbf{\Psi}\boldsymbol{\alpha} \tag{5}$$

Here $\mathbf{x} \in \mathbb{R}^{p \times 1}$ is the observable signal vector and $\mathbf{\Phi} \in \mathbb{R}^{m \times p}$ is a measurement matrix applied to sample the measurements. The matrix $\mathbf{\Psi} \in \mathbb{R}^{p \times n}$ represents the dictionary, enabling a sparse representation $\boldsymbol{\alpha}$ of the observable signal $\mathbf{x}$.

If we consider the above formulations in the setting of reconstructing an AFM image from samples scanned on a specimen, $\mathbf{y}$ corresponds to the scanned samples of the image $\mathbf{x}$, a vector version of $\mathbf{X}$. We wish to reconstruct an estimate $\hat{\mathbf{x}}$ of the image from $\mathbf{y}$. The fact that $m < p \leq n$ means that (3), or equivalently (4) together with (5), constitutes an under-determined linear equation system which we cannot directly invert to obtain $\hat{\mathbf{x}}$. Sparse regularisation as used in, e.g. compressed sensing enables solving (3) for $\boldsymbol{\alpha}$, and equivalently for $\mathbf{x}$ through (5), by solving the following (non-convex) optimization problem [23]:

$$\hat{\boldsymbol{\alpha}} = \arg\min_{\boldsymbol{\beta}} \|\boldsymbol{\beta}\|_0 \quad \text{s.t.} \quad \mathbf{y} = \mathbf{A}\boldsymbol{\beta} \qquad (6)$$

Unfortunately (6) is an intractably difficult combinatorial problem to solve exactly. However, compressed sensing theory shows that (6) can be replaced by the following convex relaxation of the problem [23], [26]:

$$\hat{\boldsymbol{\alpha}} = \arg\min_{\boldsymbol{\beta}} \|\boldsymbol{\beta}\|_1 \quad \text{s.t.} \quad \mathbf{y} = \mathbf{A}\boldsymbol{\beta} \qquad (7)$$

The optimization problem in (7) can solve (3) exactly under certain conditions [26], [28]. The convex relaxation in (7) is one approach to approximating a solution to (6). However, there exist a number of different approaches which we survey a selection of in Section III-B.

The reconstruction method can be generalized to the case of noisy measurements and/or signals that are not exactly sparse but rather "compressible" in the sense that they are accurately approximated by a few of the largest entries in $\boldsymbol{\alpha}$:

$$\mathbf{y} = \boldsymbol{\Phi}\mathbf{x} + \mathbf{e} \qquad (8)$$

The vector $\mathbf{e} \in \mathbb{R}^{m \times 1}$ represents noise in the acquired measurements, e.g. the impairments described in Section II-C, and/or the error resulting from sparsely approximating a signal that is not strictly sparse. In this case, the following optimization problem reconstructs the signal [26]:

$$\hat{\boldsymbol{\alpha}} = \arg\min_{\boldsymbol{\beta}} \|\boldsymbol{\beta}\|_1 \quad \text{s.t.} \quad \|\mathbf{A}\boldsymbol{\beta} - \mathbf{y}\|_2 \leq \epsilon \qquad (9)$$

The parameter ϵ bounds the 2-norm of the error $\mathbf{e}$.

The sparse representation model (5) is known as the sparse synthesis model – for its ability to synthesize a signal $\mathbf{x}$ from a sparse vector $\boldsymbol{\alpha}$. This model also has a counterpart: the co-sparse analysis model [29]:

$$\boldsymbol{\alpha} = \boldsymbol{\Psi}^{\top}\mathbf{x} \qquad (10)$$

This model admits a sparse representation of the signal $\mathbf{x}$ after multiplication by an analysis dictionary $\boldsymbol{\Psi}^{\top}$. Note here that good dictionaries for the analysis model are not necessarily simply a transpose of a corresponding synthesis dictionary, but we use this notation here in order not to complicate the notation with additional symbols. The optimization problem for reconstructing $\mathbf{x}$ from the analysis model, as a counterpart to (9) can be stated as:

$$\hat{\mathbf{x}} = \arg\min_{\tilde{\mathbf{x}}} \|\boldsymbol{\Psi}^{\top}\tilde{\mathbf{x}}\|_1 \quad \text{s.t.} \quad \|\boldsymbol{\Phi}\tilde{\mathbf{x}} - \mathbf{y}\|_2 \leq \epsilon \qquad (11)$$

A number of theoretical conditions for compressed sensing reconstruction to succeed can be found in the literature [26],

[30], but most of the theory relies on the measurement matrix $\boldsymbol{\Phi}$ having i.i.d. random entries. A random measurement matrix is difficult to achieve when scanning a specimen in an efficient manner in AFM and further, the continuous trajectory typically used in AFM in this case violates the assumption of i.i.d. entries. Therefore, the imaging techniques explored in this paper are not strictly compressed sensing. Nevertheless, we investigate some of the reconstruction algorithms known especially from compressed sensing to assess the value of reconstructing images in AFM by sparse approximation.

Previous work has shown that for particular AFM images having much greater energy in the high-frequency domain than in the low-frequency domain, sparse approximation techniques generally perform better than (Delaunay) interpolation-based techniques, whereas for low-frequency AFM images, excellent performance can be obtained with Delaunay interpolation [31].

A. Measurement and Dictionaries

As mentioned in Section III, the sensing matrix $\mathbf{A}$ can be considered as the product of a separate measurement matrix $\boldsymbol{\Phi}$ and (synthesis) dictionary matrix $\boldsymbol{\Psi}$ where the purpose of the measurement matrix is to represent the process that physically measures the sample. The purpose of the dictionary matrix is to enable a sparse representation of the image $\mathbf{x}$.

When considering separate measurement matrices $\boldsymbol{\Phi}$ and dictionaries $\boldsymbol{\Psi}$, the matrices should be selected from incoherent orthogonal bases Φ and Ψ. Coherence, μ, is a measure of the similarity of the vectors Φ and Ψ [26]. A low coherence is better. The measurement matrix $\boldsymbol{\Phi}$ should consist of rows selected uniformly at random from Φ while the columns of the dictionary matrix $\boldsymbol{\Psi}$ should be the vectors from Ψ [26]. The preceding descriptions apply to the case of a dictionary $\boldsymbol{\Psi}$ corresponding to an orthonormal basis [32], i.e. $m = p$ in (5). However, the more general case of over-complete dictionaries where $m < p$ is also possible [33].

An overview of the past and present directions in the design of dictionaries is given in [34]. The possibilities range from the fixed, general purpose, orthogonal dictionaries over more adapted over-complete dictionaries [35], [36] to the highly data- and application-specific dictionaries designed using a Karhunen-Loeve transform [37] (also known as a PCA transform [38]) or a learning approach [39], [40]. Although any of these approaches may be applicable for AFM image representation, here we only discuss fixed dictionaries such as the discrete cosine transform (DCT)[2] or the discrete wavelet transform (DWT). These transforms are of particular interest due to their simplicity, their celebrated applicability in general compressive imaging [27], and the availability of efficient implementations requiring only $\mathcal{O}(n \log(n))$ computations as well as relaxed memory requirements due to an implicit representation of the dictionary matrix [41].

The DCT is used in the JPEG coding standard [42] and as such is known to be successful in sparsely representing

---

[2]Here we consider the DCT as a representative of the family of sinusoidal transforms which also includes, e.g. the discrete Fourier transform (DFT). It is our experience that the use of the DFT gives reconstructions comparable to those based on the DCT.

smooth images. However, in JPEG the DCT dictionary is used on smaller patches of the image whereas we only apply dictionaries to the full image in this study. In terms of its applicability in AFM imaging, the DCT is the dictionary used in two independent recent studies on the applicability of compressed sensing in AFM [31] and SEM [43]. The DWT is generally very successful in sparsely representing piece-wise smooth images. Consequently, it is the transform chosen in the JPEG2000 coding standard [44]. The DWT has been successfully used in a number of compressive imaging studies, see e.g. [45] and [46]. Note, however, that these studies use dense sampling matrices with random entries and not the sparse point sampling used in AFM.

The excellent sparse representation capabilities of the DCT and DWT on natural images make them both good candidates for use in reconstruction of undersampled AFM images. We have, however, found that the DWT can be problematic when used in combination with point sampling. As (4) shows, mea-surements in compressed sensing are generally random linear combinations of the entries of the observable signal. In AFM, however, the physical properties of the probe tip only allow the microscope to sample the specimen in discrete points, i.e. each row in $\boldsymbol{\Phi}$ contains only *one* 1-entry while the other entries are 0, making this point sampling measurement matrix extremely sparse. The DWT dictionary matrix is relatively sparse compared to the DCT and it follows that their product is likely to be sparse, where some columns can become all-zero. Thus, the null-space of the product matrix is non-empty and there exist sparse solutions which cannot be represented by the particular pair of measurement and dictionary matrix. Intuitively, the DWT basis functions are not able to smoothly interpolate between points spaced too far apart due to being very localized in the image domain. Hence, we may experience low incoherence between the DWT and point sampling. This is not the case for the DCT dictionary matrix, which is dense and maximally incoherent with point sampling [26]. To demonstrate the difference in reconstruction capabilities between DCT and DWT dictionaries, we include results of experiments with both dictionary types in Section IV. As the results show, the performance depends strongly on the type of sampling pattern used.

B. Reconstruction Algorithms

In the following, we review a number of reconstruction algorithms that can be used to reconstruct undersampled AFM images by sparse approximation.

1) Convex Optimization: The classic approach to solving sparse approximation problems described by (6) is using the ℓ_1 norm convex optimization formulations introduced by (7) and (9). The constrained convex formulation (9) is also com-monly found in a regularized form:

$$\hat{\boldsymbol{\alpha}} = \arg\min_{\boldsymbol{\beta}} \left\{ \tau\|\boldsymbol{\beta}\|_1 + \frac{1}{2}\|\mathbf{A}\boldsymbol{\beta} - \mathbf{y}\|_2^2 \right\} \qquad (12)$$

Although (12) appears different from (9) at first glance, they can produce identical solutions for given pairs of (ϵ, τ) [47]. These convex optimization formulations are also known as

the least absolute shrinkage and selection operator (LASSO) or basis pursuit de-noising (BPDN) [48], [49].

Equations (7), (9), (12) are formulations of the problem to solve. However, various different algorithms can be employed to compute the actual solution [50], [51]. Some solvers for this type of problems are implemented in for example PyUN-LocBoX[3] [52], SPGL1[4] [53], YALL1[5] [54], and TFOCS[6].

Another convex optimization method following the ap-proach in (11) is using total variation (TV) minimization [55]. Proposed for image denoising in the context of image pro-cessing [56], TV is a measure that quantifies the variation in some function. In image reconstruction, the TV measure is used to minimize the variation in the reconstructed image. That is, this approach takes advantage of the fact that natural images tend to consist of relatively large smooth regions and exploits this fact to fill in missing regions between the known parts of the image. Anisotropic TV can be seen as analysis co-sparse approximation with a discrete difference operator as the analysis dictionary, see (10). The anisotropic TV operator can be found in, e.g. [57]. As an example of analysis-based sparse approximation, we apply a slightly different variant; isotropic TV. This has also been applied to AFM image reconstruction in [7]. A related application is found in [58] where a slightly different but similar approach known as heat equation in-painting is used. The isotropic TV convex optimization problem can be posed as [59]:

$$\hat{\mathbf{x}} = \arg\min_{\mathbf{x}} \mathrm{tv}(\mathbf{x}) \quad \text{s.t.} \quad \|\boldsymbol{\Phi}\mathbf{x} - \mathbf{y}\|_2 \le \epsilon \qquad (13)$$

In (13), we have used vector notation for the image $\mathbf{x}$ to sim-plify the constraint. For the purposes of numerical computation used in image processing, a discrete approximation of the TV norm is used since the image is discretized to a pixel grid. One definition of this discretization can be found in [59]:

$$\mathrm{tv}(\mathbf{X}) = \sum_{k=0}^{h-2}\sum_{l=0}^{w-2}\left(\left|\mathbf{X}_{(k+1,l)} - \mathbf{X}_{(k,l)}\right|^2 + \right.$$

$$\left.\left|\mathbf{X}_{(k,l+1)} - \mathbf{X}_{(k,l)}\right|^2\right)^{\frac{1}{2}} + \sum_{k=0}^{h-2}\left|\mathbf{X}_{(k+1,w-1)} - \mathbf{X}_{(k,w-1)}\right|^2$$

$$+ \sum_{l=0}^{w-2}\left|\mathbf{X}_{(h-1,l+1)} - \mathbf{X}_{(h-1,l)}\right|^2 \qquad (14)$$

In (14), we have used matrix notation for the image $\mathbf{X}$ to simplify indexing; $\mathbf{X}_{(k,l)}$ indexes the (k,l)'th entry in $\mathbf{X}$. Equation (14) is the isotropic version of the discrete TV norm.

The problem (13) can be solved using different algorithms such as split Bregman [60] or Douglas-Rachford splitting [52], [61]. Implementations of algorithms solving TV optimization can be found in PyUNLocBox, which can solve (13) as described in [62]. TFOCS[6] [63] also implements a solution.

2) Greedy Pursuits: An alternative to the convex optimiza-tion based reconstruction algorithms is using the class of so-called *greedy* reconstruction algorithms. The term *greedy* is

---

[3]Available at https://github.com/epfl-lts2/pyunlocbox.
[4]Available at http://www.cs.ubc.ca/labs/scl/spgl1.
[5]Available at http://yall1.blogs.rice.edu/.
[6]Available at http://cvxr.com/tfocs/.

used because these algorithms iteratively take decisions that are locally optimal in each iteration [64].

Generally, an iteration of a greedy algorithm involves a greedy selection of support elements (columns of $\mathbf{A}$) followed by a coefficient update (an update of $\hat{\boldsymbol{\alpha}}$), see e.g. [64, Algorithm 8.1]. The simplest examples are so-called greedy pursuits like Matching Pursuit (MP) [35] or Orthogonal Matching Pursuit (OMP) [65] that only allow for a continued increase of the support. Algorithms like Iterative Hard Thresholding (IHT) [66] or Iterative Soft Thresholding (IST)[7] [67] have an ability to also prune elements from the support. For common parameter choices, the IHT interchanges the optimization criterion and the constraint in (9) and uses the ℓ_0 pseudo-norm from (6) instead of the ℓ_1 relaxation:

$$\hat{\boldsymbol{\alpha}} = \arg\min_{\boldsymbol{\beta}} \|\mathbf{A}\boldsymbol{\beta} - \mathbf{y}\|_2 \quad \text{s.t.} \quad \|\boldsymbol{\beta}\|_0 \leq k \qquad (15)$$

In particular the IHT and IST algorithms have a simple iterative form which can be written (with iteration index k) as:

$$\boldsymbol{\beta}^{(k+1)} = \mathrm{T}_\mu \left(\boldsymbol{\beta}^{(k)} + \kappa \mathbf{A}^\top \left(\mathbf{y} - \mathbf{A}\boldsymbol{\beta}^{(k)} \right) \right) \qquad (16)$$

The parameter κ is a step size. The function T_μ is a thresholding operator applied entry-wise to each of the entries v of a vector $\mathbf{v}$. For IHT the hard thresholding operator [66] is:

$$\mathrm{T}_\mu(v) = \begin{cases} 0 & \text{for } |v| \leq \mu \\ v & \text{otherwise} \end{cases} \qquad (17)$$

For IST the soft thresholding operator [67] is:

$$\mathrm{T}_\mu(v) = \begin{cases} 0 & \text{for } |v| \leq \mu \\ \mathrm{sgn}(v)\,(|v| - \mu) & \text{otherwise} \end{cases} \qquad (18)$$

Even more advanced algorithms exist such as Subspace Pursuit [68] or CoSaMP [69] that introduce a two-stage thresholding scheme with an intermediate support element selection and coefficient update.

Although some of the greedy algorithms can be shown to have theoretical recovery guarantees that match those of the ℓ_1 based convex relaxation methods [64], empirical evidence suggests that they do not perform as well as ℓ_1 optimization [70], [71]. The greedy algorithms are, however, worth considering due to their low computational complexity. The computational cost in an iteration of e.g., MP, IHT, or IST is dominated by the computation of matrix-vector products involving $\mathbf{A}$ and $\mathbf{A}^\top$, thus, having complexity $\mathcal{O}(n^2)$. If fast transforms are available, as is the case when using e.g. the DCT as described in Section III-A, the computational cost is $\mathcal{O}(n \log(n))$. This has a significant impact on the time it takes to do the reconstruction for large problem sizes such as a $256 \times 256 = 65536$ pixels AFM image.

3) Approximate Message Passing: Probabilistic Message Passing (MP) algorithms based on graphical belief models are known from Bayesian inference used in machine learning [72]. This is an advanced method of reconstruction, which takes into account prior information the user may have on

---

[7]IST can also solve a variant of the ℓ_1 minimization problem and as such is not completely distinct from them.

---

signal characteristics [73]. It unfortunately suffers from severe computational load and may also show poor convergence properties if the algorithmic assumptions are not fulfilled [74]. The Approximate Message Passing (AMP) algorithm is derived as a first order approximation, which reduces the computational burden significantly [72], [75]–[77]. AMP exists in several variants allowing different signal priors [78], inclusion of parameters as variables [79] etc. The following is based on a reasonably simple AMP method using a Bayesian framework for probabilities. Maleki and Baraniuk [80] showed links between AMP and Iterative Soft Thresholding (IST) in terms of identical convergence properties, and it has also been shown that the AMP algorithm can solve the LASSO (Least Absolute Shrinkage and Selection Operator) problem formulated in (12) [79].

The Minimum Mean-Square Error (MMSE) signal reconstruction estimate for x_n can be found from a marginal Bayesian mean of the posterior marginal estimate as [81]:

$$\hat{x}_n^{\mathrm{MMSE}} = \int_{x^*} x_n\, \wp_{X|Y}(x_n|\mathbf{y})\, \mathrm{d}x_n \qquad (19)$$

where $\wp_{X|Y}(x_n|\mathbf{y})$ is the conditioned posterior pdf (probability density function), and x^* is the space of x_n. To compute the MMSE estimate in (19) we need to determine the conditioned posterior probability $\wp_{X|Y}(x_n|\mathbf{y})$, which can be done via Bayes' rule [81]:

$$\wp_{X|Y}(x|y) = \frac{\wp_{Y|X}(y|x)\, \wp_X(x)}{\wp_Y(y)} \qquad (20)$$

$$= \frac{\wp_{Y|X}(y|x)\, \wp_X(x)}{\int_{x^*} \wp_{Y|X}(y|x)\, \wp_X(x)\, \mathrm{d}x} \qquad (21)$$

For the sparse input signal $\mathbf{x}$ we assume all components to be i.i.d. Bernoulli-Gaussian with marginal pdf:

$$\wp_X(x_n) = \rho\, \mathcal{N}(x_n; \mu_{\mathrm{x}}, \sigma_{\mathrm{x}}^2) + (1 - \rho)\, \delta_{\mathrm{dirac}}(x_n) \qquad (22)$$

where $\rho \in [0; 1]$, $\delta_{\mathrm{dirac}}(\cdot)$ is the Dirac δ-function [82], and the general Gaussian function is:

$$\mathcal{N}(x_n; \mu_{\mathrm{x}}, \sigma_{\mathrm{x}}^2) = \frac{1}{\sqrt{2\pi}\,\sigma_{\mathrm{x}}} \exp\left(\frac{-(x_n - \mu_{\mathrm{x}})^2}{2\,\sigma_{\mathrm{x}}^2} \right) \qquad (23)$$

The noise in (8) is modeled as additive white Gaussian noise with a pdf given by:

$$\wp_E(e_n) = \mathcal{N}(e_n; 0, \sigma_{\mathrm{e}}^2) \qquad (24)$$

The Message Passing (MP) is then included to describe the steps:

$$\boldsymbol{\alpha} \rightarrow \mathbf{z} = \mathbf{A}\,\boldsymbol{\alpha} \rightarrow \mathbf{y} = \mathbf{z} + \mathbf{e} = \mathbf{A}\,\boldsymbol{\alpha} + \mathbf{e} \qquad (25)$$

remembering that $\mathbf{x} = \boldsymbol{\Phi}\boldsymbol{\alpha}$. When $\wp_X(x)$ is unknown, the expression above represents an assumption of the pdf. Other pdfs may be used such as Laplace and Bernoulli-Gaussian Mixture models [79]. The output can be based on any separable distribution. In the special case of a Laplace pdf, the algorithm can be reduced to a simple thresholding algorithm similar to (16) with an additional correction term in the argument to the threshold operator (18). The algorithmic complexity of the AMP algorithm based on Bernoulli-Gaussian input prior and Gaussian output prior is $\mathcal{O}(m\,n)$.

4) Reference Method: Interpolation: Interpolation using irregularly spaced samples is a widely studied topic and used in diverse disciplines such as signal processing [83], [84], computational geometry [85], and geoscience [86]. Here The computationally simplest approaches to interpolation are nearest neighbor interpolation, where the nearest known pixels are simply copied to the unknown pixel locations, and linear interpolation, where nearby pixels are linearly combined to provide the values for the missing pixels. The weights used in the linear combination are often empirically chosen such that an average of the neighboring pixels is obtained or they depend upon the distance between the pixels as is the case with Kriging linear interpolation [86]. The weights can also be analytically chosen to satisfy e.g., well-established sampling theorems in shift-invariant spaces such as non-uniform interpolation with b-splines [87] and sinc kernels [88]. Another common approach is to use Delaunay triangularization, where the surface area is subdivided into non-overlapping triangles. The vertices of the triangles are assigned the measured points, and any point within a triangle can be obtained by (non)-linear interpolation methods such as linear, cubic, and nearest-neighbor interpolation between its three vertices [85]. In this study we use the latter interpolation method as a reference to compare the sparse approximation methods against.

IV. EXPERIMENTS

In order to give an overview of the possibilities of image reconstruction from sparsely sampled images we have conducted an extensive set of experiments to showcase the capabilities of different reconstruction approaches presented in Section III. The experiments cover basic variants of the involved reconstruction algorithms, i.e., no attempts were made to exploit special structure in the images or apply dictionary learning etc. It is therefore also likely that specialization of the algorithms may offer further reconstruction quality improvements or mitigation of some of the impairments described in Section II-C.

A. Quality Indicators

In order to assess the reconstruction quality in the experiments, we apply two standardized image quality indicators. The first is peak signal-to-noise ratio (PSNR):

$$\text{PSNR} \; = \; 10 \log_{10} \left(\frac{P^2}{\sum_{k=0}^{h-1} \sum_{l=0}^{w-1} \left(\mathbf{X}_{(k,l)} - \hat{\mathbf{X}}_{(k,l)} \right)^2} \right) \tag{26}$$

The value P is the maximum possible value of a pixel in $\mathbf{X}$, i.e. $P = 1$ according to the numeric representation of the images described in Section IV-C.

The second metric is the structural similarity (SSIM) index which we use according to the definition in [89]. In particular, we use: window size 7, $K_1 = 0.01$, $K_2 = 0.03$, $C_3 = \frac{C_2}{2}$, and $\alpha = \beta = \gamma = 1$, cf. [89, Eq. (13)].

All reconstructed images are scaled to have pixel values in the range $[0, 1]$ prior to application of the PSNR and SSIM indicators.

The color map referred to as "cool-warm" in [90] (exemplified in Figure 1a) is used for visualizing the ground truth images in Figure 2 as well as the reconstructed images. We have found through perceptual evaluation of the ground truth images that this color map is better for discerning image details otherwise lost in the color map traditionally applied in AFM imaging which is exemplified in Figure 1b.
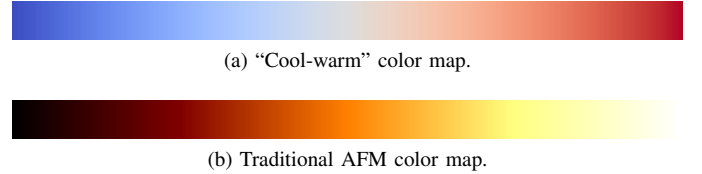

(a) "Cool-warm" color map.

(b) Traditional AFM color map.

Fig. 1. Color maps for visualization of images.

B. Sampling Pattern

We investigate reconstruction performance under varying density of the applied sampling pattern. The density of the sampling pattern is expressed in terms of an undersampling ratio defined as follows: the undersampling ratio is measured with respect to the length of the scan path as this can reasonably be assumed proportional to the amount of time required to scan the image. We take as reference scan path length the length of the dense raster pattern used to scan the original images in Figure 2. This reference length is approximated as:

$$L_{\text{ref}} \; = \; 2 \, w \, h \tag{27}$$

That is, the length of each horizontal line w times the number of lines h, expressed in pixels. The multiplication by 2 stems from the fact that the probe is scanned both back and forth once in each direction for each line counted. This in principle results in two images; one composed of the left-to-right-scanned samples and one composed of the right-to-left-scanned samples. Only one of these images is used as they are usually equivalent (but not completely identical) for practical purposes. The undersampling ratio δ is finally calculated as

$$\delta \; = \; \frac{L}{L_{\text{ref}}} \tag{28}$$

The length L is the length of the applied sampling pattern in units of pixels. In reconstruction experiments involving the spiral sampling pattern, we have simulated a scan path that scans beyond the square region of the original image until the spiral pattern fills the corners of the square as can be seen in Figure 2h. In calculating the resulting undersampling ratio, we also include the parts of the spiral scan path outside the square image region for fairness of comparison. This is done because the AFM equipment would have to traverse these unused regions outside the image region in order not to introduce scanning artifacts by deviating from the smooth curve of the spiral path. Note that (28) is not equal to the undersampling ratio measured in image pixels and (28) reflects the fact that we wish to focus on the potential time savings in applying sparse sampling patterns in AFM.

(a) Chinese hamster ovary cells.   (b) Chinese hamster ovary cells.   (c) Human bladder carcinoma cells.   (d) Human bladder carcinoma cells.

(e) Chinese hamster ovary cells.   (f) Chinese hamster ovary cells.   (g) Chinese hamster ovary cells.   (h) Sampling pattern example.
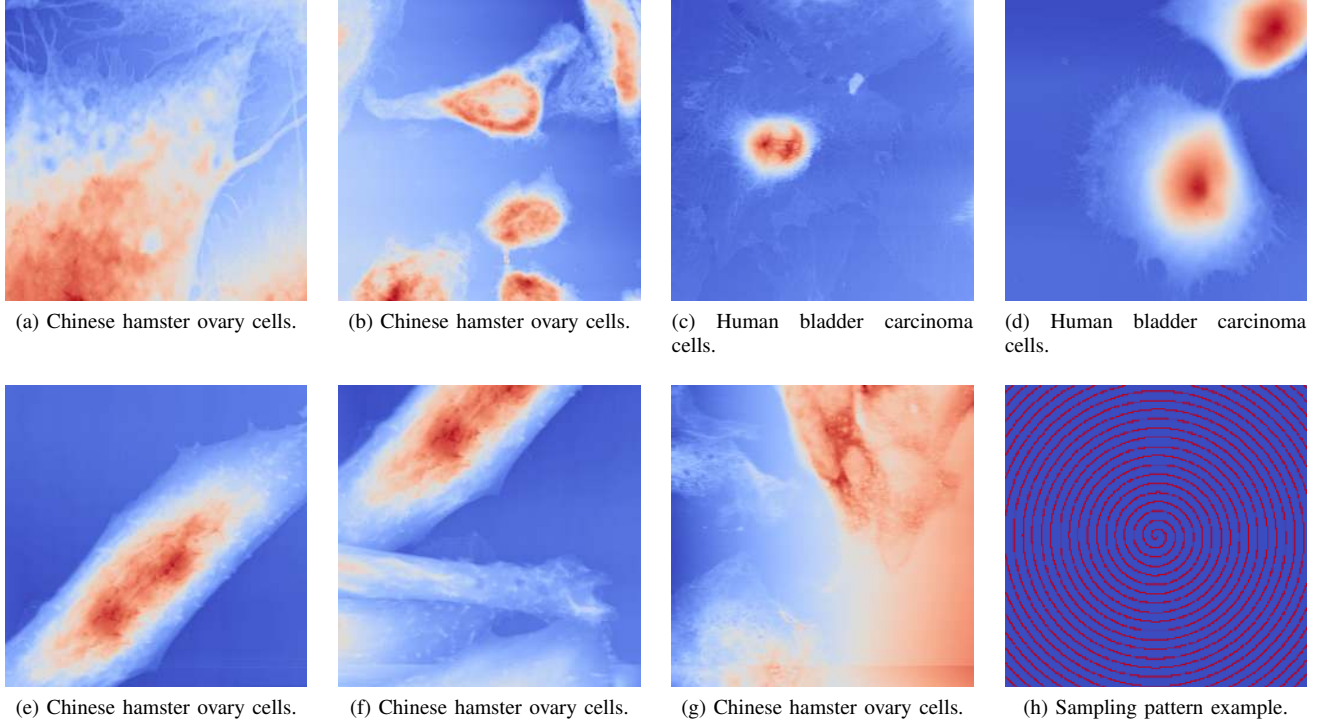
Fig. 2. (a)–(g) The seven ground truth images used in reconstruction experiments here shown before de-tilting; (h) shows an example of the spiral sampling pattern with $\delta = 0.1$.

C. Image Material

As examples of cell images we have selected the seven images shown in Figure 2. The images have originally been scanned for a size of 512×512 pixels, but have been subsequently decimated to 256×256 pixels to reduce the computational complexity of the reconstruction[8]. The images are stored and processed as double precision (64-bit) floating point values in the interval $[0, 1]$. Images (a), (c), (e), and (f) have been acquired in acoustic AC mode; images (b), (d), and (g) have been acquired in contact mode. The images have been acquired on Keysight Technologies ILM6000 and 7500 AFM equipment. The original image files are available along with this paper[9].

We demonstrate the performance of the reconstruction algorithms on images sampled using raster-, respectively, spiral-shaped scanning paths. In the experiments, we did not have access to images scanned along a spiral scan path. For this reason, the measurements used in the reconstruction experiments were constructed as follows: the original images were acquired using a dense raster scan path with one line per line of pixels in the resulting image; spiral-scanned measurements were simulated by picking pixels from the original images in a spiral-shaped pattern as illustrated in Figure 2h; for fairness of comparison, the raster-scanned measurements used in the experiments were similarly picked as horizontal lines–joined at the ends by vertical segments–of pixels from the original

[8]Most of the tested algorithms can actually handle images of size 512×512, but the Bernoulli-Gaussian AMP algorithm described in Section III-B3 was unable to handle larger images on the available hardware due to memory requirements.

[9]http://dx.doi.org/10.5281/zenodo.17573

images. The undersampling ratio defined in Section IV-A is varied among the following values:

$$\delta \in \{0.1 + n \cdot 0.025 \mid n = 0, 1, \ldots, 8\} \qquad (29)$$

In the reconstruction experiments, the images have been de-tilted prior to reconstruction. This is done by least-squares-fitting a plane through the available measurements according to the applied sampling pattern. The fitted plane is then subtracted from the measurements. When evaluating PSNR or SSIM of the reconstructed images, the reconstructed images are compared to the de-tilted original.

There was not sufficient information available regarding the physical experimental set-up used in producing the images in Figure 2 to analyze and estimate the amount of measurement noise in the images as described in, e.g. [19]. When available, such estimates of measurement noise should be included appropriately in the reconstruction algorithms. For example, in the cases of (13) and (9) the estimated noise variance can be used to determine ϵ.

D. Algorithm Implementations

For each of the sampling patterns (raster or spiral) and each of the undersampling ratios, we reconstruct each of the seven images using the following reconstruction algorithms: ℓ_1-minimization (Section III-B1), AMP – with Laplace prior and with Bernoulli-Gaussian prior (Section III-B3), IST and IHT (Section III-B2), TV minimization (Section III-B1), cubic interpolation via Delaunay triangulation (Section III-B4). The simulation code has been implemented in Python, which is a popular, open and suitable ecosystem for scientific computing

(a) Spiral sampling pattern
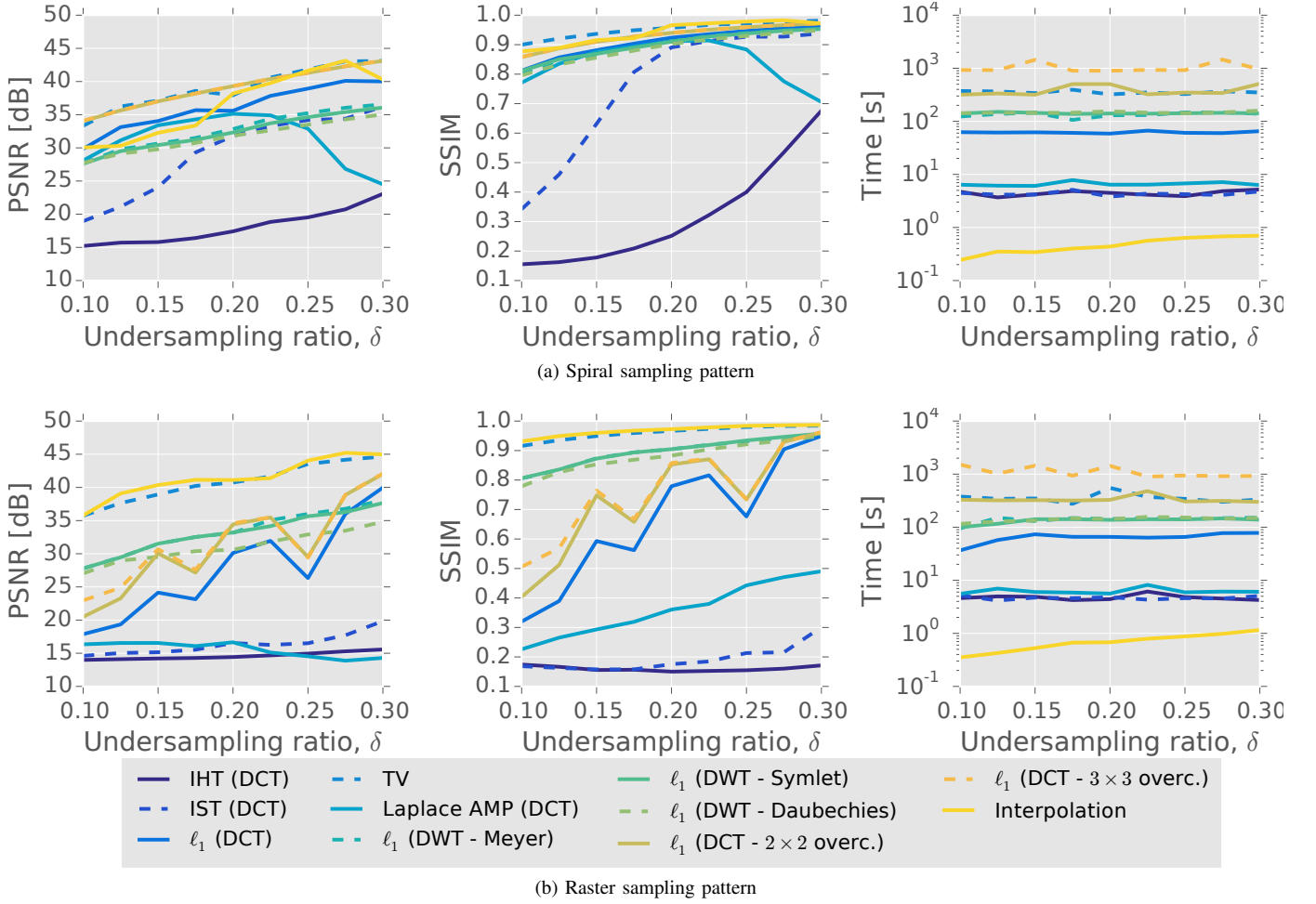
(b) Raster sampling pattern

Fig. 3. Comparison of reconstruction PSNR, SSIM, and run-time across the tested reconstruction algorithms, at 256×256 pixels.

[91], [92]. Python also supports the ideas of reproducible research which are considered important in the present simulation rich context [93], [94]. The complete Python code used to conduct the reconstruction experiments is available along with its results[10]. Interaction with the data files from the AFM equipment, generation of sampling patterns, measurement and dictionary matrices (for the algorithms utilizing the latter) as well as evaluation of quality indicators and visualization of reconstruction results are handled through the Magni software package[11] described in [95]. Some of the applied reconstruction algorithms are provided as part of the Magni package while others are available in other packages; see details in the following:

1) *ℓ_1-minimization* For reconstruction via ℓ_1 minimization, we solved (9). Reconstructions using ℓ_1-minimization were performed using an orthogonal DCT dictionary as well as over-complete DCT dictionaries. The over-complete dictionaries applied 2 and 3 times oversampling along each dimension of the frequency domain. This amounts to a total of 4 and 9 times oversampling, respectively. The over-complete DCT dictionaries were implemented by applying zero-padding in the image domain. Additionally, reconstructions using ℓ_1-minimization were performed using orthogonal DWT dictionaries with three different types of wavelets: Meyer, Daubechies, and symlets. All three wavelet types were used in their longest available form in the PyWavelets toolbox for Python[12]. Wavelets with the longest available filters were chosen to mitigate possible problems with measurement-dictionary coherence and non-empty null-space discussed in Section III-A.

The solver iterates until the constraint in (9) is met or a limit of 2000 iterations has been reached. Other settings in the solver may influence the stopping conditions; these have been left at their standard values.

2) *Approximate Message Passing* For reconstruction via AMP, we have implemented the algorithm in Python for a Laplace as well as a Bernoulli-Gaussian (BG) prior. The code is included in the software accompanying this paper. The algorithms are iterated until they reach an upper limit of 300 iterations or if the residual:

$$\|\mathbf{y} - \mathbf{A}\,\hat{\boldsymbol{\alpha}}\|_2 < \epsilon \|\mathbf{y}\|_2, \quad \epsilon = 10^{-3} \qquad (30)$$

Our current implementation of Bernoulli-Gaussian AMP (BG-AMP) cannot handle images in 256×256 pix-

[10]http://dx.doi.org/10.5281/zenodo.32959 and .../zenodo.32958.
[11]http://dx.doi.org/10.5278/VBN/MISC/Magni

[12]https://github.com/PyWavelets/pywt
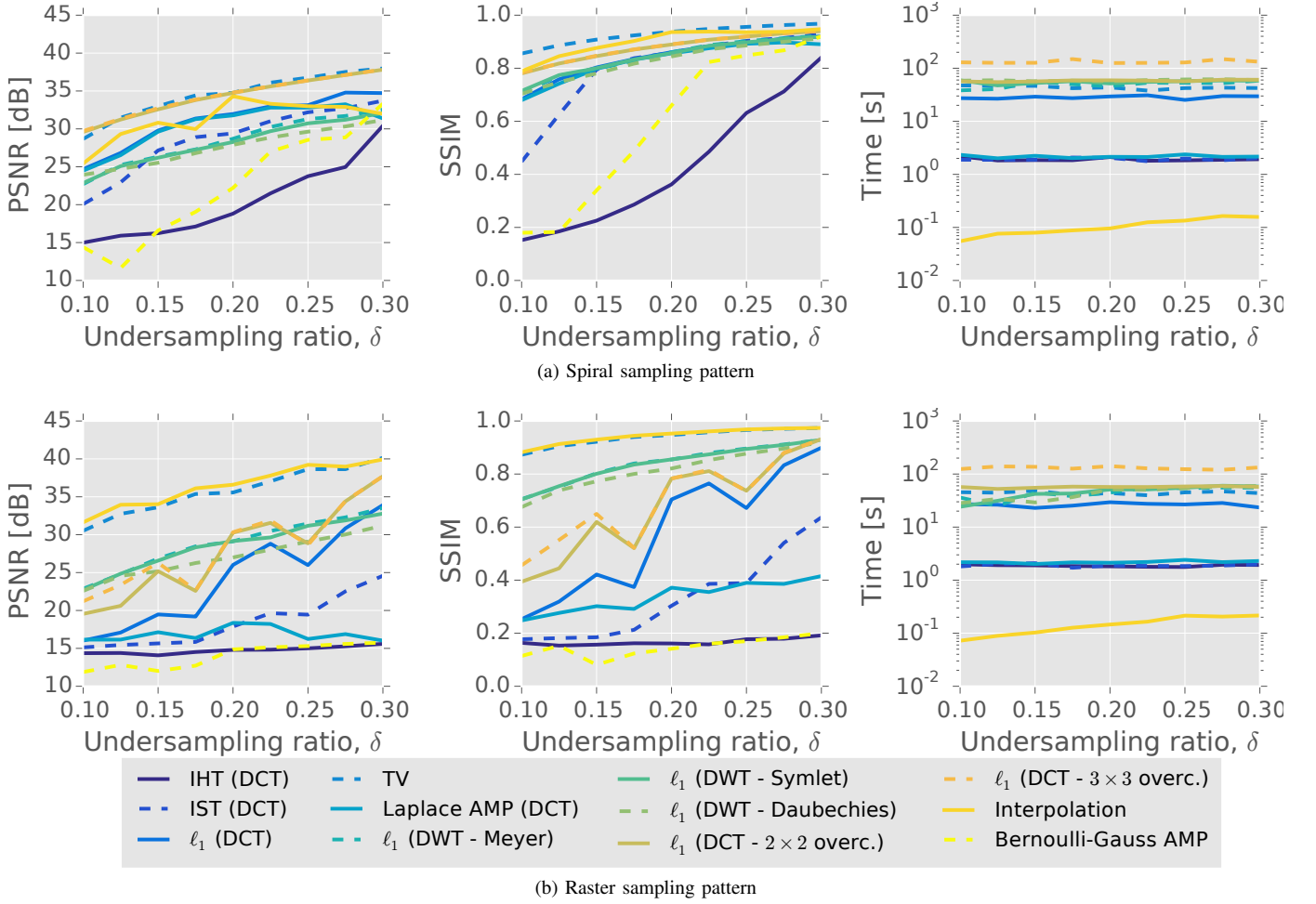
(a) Spiral sampling pattern

(b) Raster sampling pattern

Fig. 4. Comparison of reconstruction PSNR, SSIM, and run-time across the tested reconstruction algorithms, at 128×128. This figure serves to compare BG-AMP to the other algorithms.

els due to severe memory requirements. Therefore our experiments with this particular algorithm have been conducted with the images in Figure 2 decimated to 128×128 pixels. All experiments with the other algorithms have additionally been repeated at this image size for the purpose of comparison with this algorithm. Reconstructions using AMP were only performed using an orthogonal DCT dictionary.

3) *Iterative Soft and Hard Thresholding* For reconstruction via IST as well as IHT, we have implemented these algorithms in Python. The code is included in the software accompanying this paper. The algorithms are iterated until they reach an upper limit of 300 iterations or meet the condition in (30).

Reconstructions using IHT and IST were only performed using an orthogonal DCT dictionary.

4) *Total Variation* For reconstruction via TV minimization, we solved (13) using Douglas-Rachford splitting. We used the solver implemented in the PyUNLocBox package for Python, referenced in Section III-B1. The solver iterates until the constraint in (13) is met or a limit of 2000 iterations has been reached. Other settings in the solver may influence the stopping conditions; these have

been left at their standard values.

5) *Interpolation* For reconstruction via interpolation, we used cubic Bezier polynomial interpolation over triangles formed by triangulating the available measurements Φx as implemented in the `scipy.interpolate` Python module [96].

For the convex optimization-based reconstruction approaches (items 1 and 4 above) we have repeated the reconstructions over a wide range of the regularization parameter ϵ and selected the reconstructions with highest PSNR/SSIM, averaged over all images for each algorithm and undersampling ratio δ. Similarly for the IHT and IST algorithms, we repeated the reconstructions over a wide range of the sparsity parameter k and selected the reconstructions with highest PSNR/SSIM, averaged over all images for each algorithm and undersampling ratio δ. This was done in order to provide a fair basis for comparison between the different algorithms since the measurement noise is unknown and thus unavailable to estimate ϵ, as explained in Section IV-C. Also, the images are not truly sparse – merely well approximated as such. There is thus no true parameter k available and this parameter is very problem-dependent. This choice of regularization parameters is not feasible in practice since the original image is unavailable for
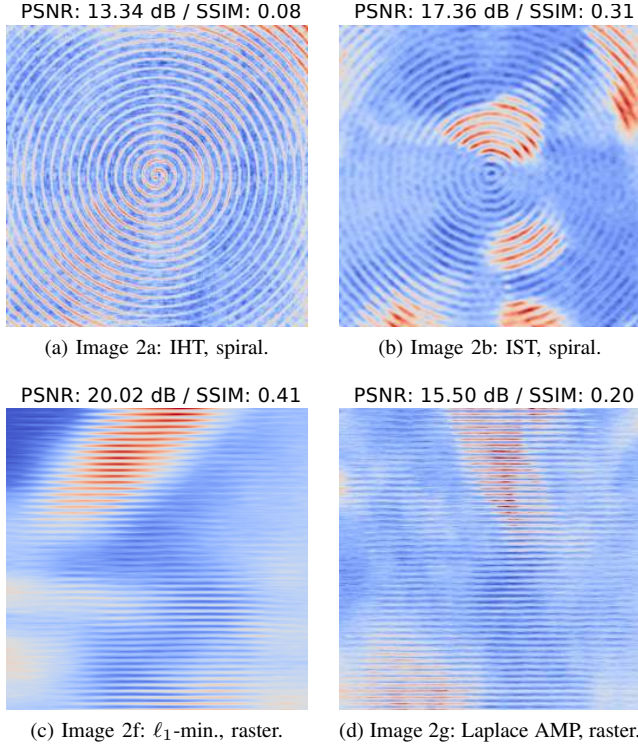
PSNR: 13.34 dB / SSIM: 0.08   PSNR: 17.36 dB / SSIM: 0.31

(a) Image 2a: IHT, spiral.   (b) Image 2b: IST, spiral.

PSNR: 20.02 dB / SSIM: 0.41   PSNR: 15.50 dB / SSIM: 0.20

(c) Image 2f: ℓ_1-min., raster.   (d) Image 2g: Laplace AMP, raster.

Fig. 5. Examples of low-quality reconstructions at $\delta = 0.1$. Images reconstructed from measurements of the ground truth images 2 (a), (b), (f), and (g). 256×256 pixels.

evaluating the reconstruction quality. It was however chosen in order to compare the mentioned algorithms on an equal footing.

For each reconstruction experiment we have measured the reconstruction time as a practical indicator of the run-time complexity. Reconstruction time can of course vary depending on the specific algorithm and the implementation of it used to reconstruct the image. Our reconstruction results could thus possibly be reproduced with different measured run-times. However, the measured reconstruction times provide a useful indicator of what is practically achievable.

V. RESULTS

For each of the reconstruction approaches, the performance in terms of both PSNR and SSIM at 256×256 pixels is plotted in Figure 3 along with reconstruction time against the tested undersampling ratios, δ. All three panels display results from the reconstructions resulting in the best PSNR among the tested regularization parameters. Figure 3a shows results for the spiral sampling pattern and 3b shows results for the raster sampling pattern, cf. Section IV-B.

As expected, reconstructed image quality in terms of PSNR as well as SSIM decreases as δ decreases. At the low undersampling end, $\delta = 0.1$, this results in reconstructions of very low PSNR/SSIM, a few examples of which are shown in Figure 5.

Figure 3 shows that interpolation and TV minimization reconstruct the images best among the tested algorithms, both in terms of PSNR and SSIM. As shown in Figure 3b,

interpolation results in the highest PSNR as well as SSIM averaged over the seven ground truth images, for the raster sampling pattern. TV reconstruction with the raster pattern results in slightly lower PSNR than interpolation, $0.6\,\mathrm{dB}$ on average. The spiral sampling pattern results in lower PSNR for both interpolation and TV minimization, $4.9\,\mathrm{dB}$ worse on average for interpolation while only $1.7\,\mathrm{dB}$ worse for TV. This also means that reconstruction by TV minimization results in $2.5\,\mathrm{dB}$ higher PSNR than interpolation for the spiral sampling pattern.

Reconstruction by ℓ_1-minimization with DCT dictionaries and the spiral sampling pattern results in the highest PSNR performance after TV optimization, where 2×2 and 3×3 overcomplete DCT result in PSNR performance close to that of TV optimization. For the spiral sampling pattern, interpolation only performs comparable to ℓ_1-minimization with orthogonal DCT dictionary. The ℓ_1-minimization with DWT dictionary performs substantially worse than for DCT dictionary with the spiral sampling pattern. Here the Meyer wavelet is slightly better than the symlet, which is again slightly better than the Daubechies wavelet. Laplace AMP exhibits a trend in PSNR performance that deviates from that of the other algorithms, deteriorating severely for $\delta > 0.2$. This is not intuitive as the algorithms have more information available for higher δ. This is likely due to unfavorable configuration of this algorithm's parameters. IST performs substantially worse than the above algorithms for $\delta < 0.2$ but comparable to ℓ_1-minimization with DWT dictionary for $\delta \geq 0.2$. Finally, IHT reconstructs at the lowest PSNR among all of the algorithms at more than $10\,\mathrm{dB}$ below ℓ_1-minimization with DWT dictionary.

The raster sampling pattern performs much worse than the spiral sampling pattern for all of the DCT dictionary-based methods (ℓ_1-minimization with DCT dictionaries, Laplace AMP, IHT and IST). IHT, IST, and Laplace AMP with the raster sampling pattern benefit very little from increased δ. The described tendencies in PSNR figures are reflected similarly in the SSIM figures. On the other hand, ℓ_1-minimization with DWT dictionaries results in PSNR as well as SSIM figures that are very close the corresponding figures for the spiral sampling pattern. Finally, both TV minimization and interpolation perform similar and best among all of the studied algorithms for the raster sampling pattern. PSNR of the latter two ranges from approximately $35\,\mathrm{dB}$ at $\delta = 0.1$ to approximately $45\,\mathrm{dB}$ at $\delta = 0.3$.

As mentioned in Section IV-D, reconstruction experiments using Bernoulli-Gaussian AMP have only been performed on images at 128×128 pixels. Figure 4 displays results of the same experiments as in Figure 3 at 128×128 pixels for comparison to BG-AMP. Data plotted in Figure 4 stems from the reconstructions resulting in the highest PSNR among the tested regularization parameters[13]. The performance of BG-AMP in terms of PSNR and SSIM lies between that of IHT and IST for the spiral sampling pattern and even slightly below IHT for the raster sampling pattern. Laplace AMP was observed to perform substantially better than BG-AMP

---

[13]The corresponding regularization parameter values are not necessarily the same as the values resulting in Figure 3.
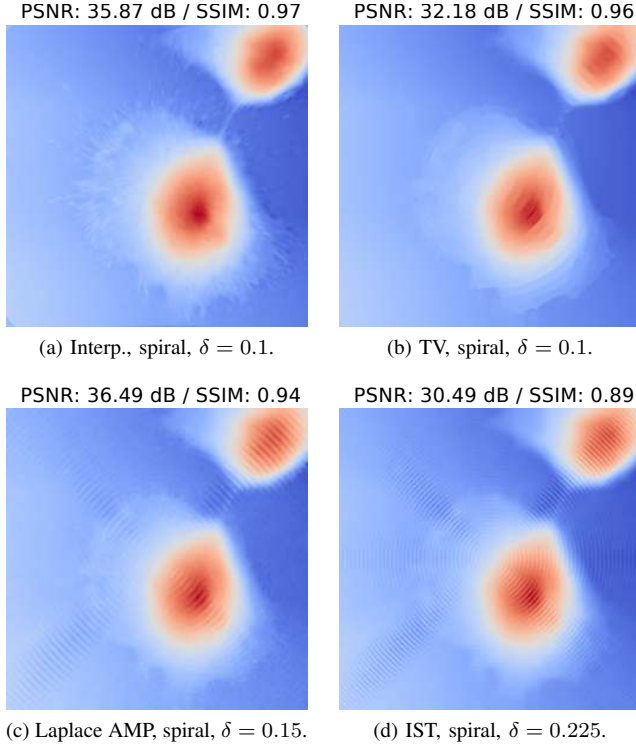
PSNR: 35.87 dB / SSIM: 0.97

PSNR: 32.18 dB / SSIM: 0.96

(a) Interp., spiral, $\delta = 0.1$.

(b) TV, spiral, $\delta = 0.1$.

PSNR: 36.49 dB / SSIM: 0.94

PSNR: 30.49 dB / SSIM: 0.89

(c) Laplace AMP, spiral, $\delta = 0.15$.

(d) IST, spiral, $\delta = 0.225$.

Fig. 6. Examples of reconstructions for the lowest δ yielding SSIM > 0.9. All images reconstructed based on measurements of the image in Figure 2d. 256×256 pixels.

PSNR: 35.08 dB / SSIM: 0.96

PSNR: 41.67 dB / SSIM: 0.97

(a) ℓ_1-min. DCT, spiral, $\delta = 0.15$.

(b) ℓ_1-min. DCT (2×2), spiral, $\delta = 0.1$.

PSNR: 41.88 dB / SSIM: 0.97

PSNR: 31.29 dB / SSIM: 0.91

(c) ℓ_1-min. DCT (3×3), spiral, $\delta = 0.1$.

(d) ℓ_1-min. DWT (Daub.), spiral, $\delta = 0.125$.

PSNR: 29.43 dB / SSIM: 0.91

PSNR: 29.43 dB / SSIM: 0.91

(e) ℓ_1-min. DWT (Meyer), spiral, $\delta = 0.1$.

(f) ℓ_1-min. DWT (symlet), spiral, $\delta = 0.1$.

Fig. 7. Examples of reconstructions for the lowest δ yielding SSIM > 0.9. All images reconstructed based on measurements of the image in Figure 2d. 256×256 pixels.

in terms of both PSNR and SSIM. A likely reason for this is that the DCT coefficients of the images have been observed to follow a probability distribution resembling the Laplace distribution rather than the Bernoulli-Gaussian. The remaining algorithms exhibit the same trends as for the 256×256 pixels images in Figure 3, except for Laplace AMP which has a much less outspoken tendency to degrade for larger values of δ than for the 256×256 pixels images.

The different reconstruction algorithms require different amounts of samples to reconstruct images satisfactorily. As examples of reconstructions of reasonable quality, we display an image reconstruction for each of the algorithms for the lowest δ that achieves a SSIM > 0.9 in Figures 6 and 7. These images represent reconstructions of somewhat degraded quality compared to the original where reconstruction artifacts typical of the tested reconstruction algorithms are evident. IHT is left out in Figures 6 and 7 since it reconstructs the image at SSIM < 0.9. BG-AMP is likewise left out since it has only been run for images at 128×128 pixels. Interpolation (Figure 6a) tends to produce artifacts that appear as if small regions of the image are smeared radially outwards from the center. Figure 6b demonstrates how TV reconstruction tends to produce reconstructions of piece-wise constant value – here particularly concentrated around the lines of the raster sampling pattern. The sparse approximation methods (Figures 6c-6d and 7a-7f) tend to leave traces of the sampling pattern in the reconstructed image, which is particularly visible in the reconstructions with DWT dictionaries: Figures 7d-7f.

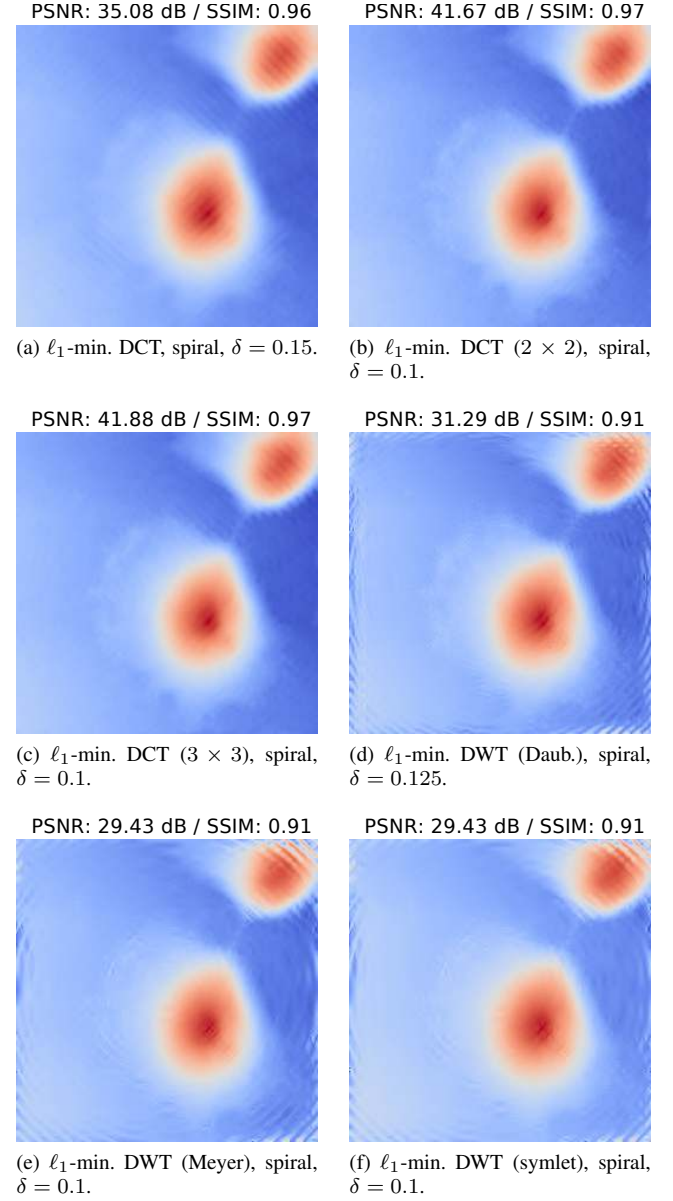To exemplify the best performance of the tested algorithms,

the best reconstruction in terms of PSNR of the image in Figure 2a is shown for each algorithm in Figure 8. All of the algorithms reconstruct the image at a legible quality but preserve finer details with varying success; interpolation and TV result in the best reconstruction quality both in terms of PSNR and SSIM (Figures 8g and 8h) while the ℓ_1 minimization algorithms with DCT dictionaries perform slightly worse (Figures 8a-8c). ℓ_1 minimization algorithms with DWT dictionaries (Figures 8d-8f) perform somewhat worse than with DCT dictionaries, producing visible edge artifacts in the reconstructed images. IHT (Figure 8k) is the only algorithm among these specific examples which leaves clearly visible sampling pattern artifacts in the reconstructed image and results in low quality.

The results indicate that reconstruction methods favoring

PSNR: 38.60 dB / SSIM: 0.95   PSNR: 39.44 dB / SSIM: 0.95   PSNR: 39.57 dB / SSIM: 0.96   PSNR: 31.90 dB / SSIM: 0.92

(a) ℓ_1-min. DCT, spiral, $\delta = 0.3$.   (b) ℓ_1-min. DCT (2×2), raster, $\delta = 0.3$.   (c) ℓ_1-min. DCT (3×3), raster, $\delta = 0.3$.   (d) ℓ_1-min. DWT (Daub.), spiral, $\delta = 0.3$.

PSNR: 35.28 dB / SSIM: 0.93   PSNR: 34.75 dB / SSIM: 0.93   PSNR: 42.93 dB / SSIM: 0.98   PSNR: 42.15 dB / SSIM: 0.98

(e) ℓ_1-min. DWT (Meyer), raster, $\delta = 0.3$.   (f) ℓ_1-min. DWT (symlet), raster, $\delta = 0.3$.   (g) Interp., raster, $\delta = 0.25$.   (h) TV, raster, $\delta = 0.3$.

PSNR: 35.68 dB / SSIM: 0.90   PSNR: 37.45 dB / SSIM: 0.94   PSNR: 24.83 dB / SSIM: 0.67

(i) Laplace AMP, spiral, $\delta = 0.225$.   (j) IST, spiral, $\delta = 0.3$.   (k) IHT, spiral, $\delta = 0.3$.
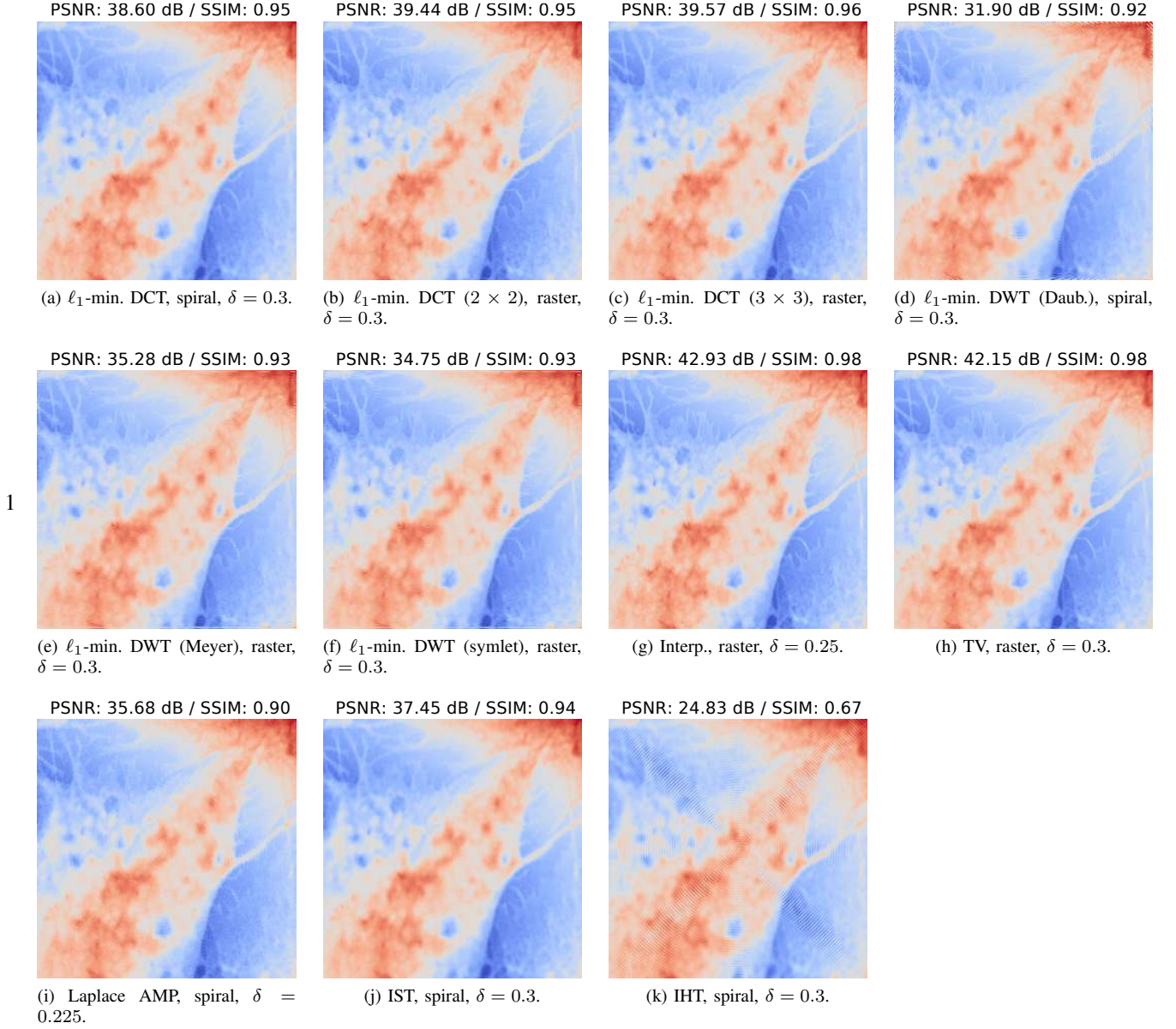
Fig. 8. Examples of reconstructions with the highest PSNR for each algorithm. All images reconstructed based on measurements of the image in Figure 2a. 256×256 pixels.

image smoothness (interpolation and TV) work slightly better than methods based on sparse approximation with DCT or DWT dictionaries. It is particularly favorable for interpolation that this method was also the fastest to compute among the tested algorithms: approximately $0.3\,\mathrm{s}$-$1\,\mathrm{s}$ depending on δ (Figure 3, right panel).

Although BG-AMP was demonstrated to work particularly poorly in the examples studied here, this type of algorithm has potential. As the Laplace variant demonstrated, selecting a more appropriate prior (Laplace) distribution of the image transform coefficients can result in better reconstruction. Furthermore, this family of algorithms can be adapted more specifically to different measurement noise distributions than for example the ℓ_1 minimization approaches and may be able to address the impairments described in Section II-C.

We stress here that the sparse approximation reconstruction

algorithms were selected to show an overview of the basic form of some popular algorithms. These sparse approximation algorithms can be specialized further to for example take advantage of image structure [97], [98], dictionary learning [40], or sparsity (ℓ_1) in an ensemble of several different dictionaries can be combined [99]. In summary, there is potential for further advances in AFM image reconstruction using sparse approximation methods.

VI. CONCLUSION

We have proposed to reduce the critical scanning time and probe-specimen interaction by AFM measurement via undersampling achieved through the use of a sparse sampling pattern. In the present study we investigated the raster sampling pattern as well as an undersampling spiral pattern; both

of varying densities. We studied the performance of a number of image reconstruction algorithms applied to measured AFM images of cell material via numerical experiments and evaluated their reconstruction performance in terms of PSNR and SSIM. We compared the central algorithms on a best-case basis over a range of different regularization parameters in order to reduce the effect of the choice of regularization parameters on the reconstruction results.

The studied algorithms include sparse approximation methods with discrete cosine transform and discrete wavelet transform dictionaries as well as total variation. These algorithms were compared to a reference method – cubic interpolation. The experimental results showed that most of the basic forms of sparse approximation algorithms studied could not quite match the reference interpolation method in terms of PSNR and SSIM. Only total variation minimization resulted in comparable PSNR and SSIM. Furthermore, interpolation was the fastest method at $0.3\,\mathrm{s}$-$1\,\mathrm{s}$ depending on undersampling ratio. Based on the tested algorithms and images, it was found that the scan time or probe-specimen interaction can be reduced by a factor of 10 compared to dense raster scanning while retaining a reconstruction PSNR $\simeq 36\,\mathrm{dB}$, or by a factor of 4 for a reconstruction PSNR $\simeq 44\,\mathrm{dB}$. These reductions in scan time / probe-specimen interaction are attainable on any existing AFM hardware capable of varying the line density of a horizontal-line raster pattern.

ACKNOWLEDGMENT

REFERENCES

[1] D. P. Allison, N. P. Mortensen, C. J. Sullivan, and M. J. Doktycz, "Atomic force microscopy of biological samples," *Wiley Interdisciplinary Reviews: Nanomedicine and Nanobiotechnology*, vol. 2, no. 6, pp. 618–634, 2010.

[2] P. Chen, H. Dong, L. Chen, Q. Sun, and D. Han, "Application of atomic force microscopy to living samples from cells to fresh tissues," *Chinese Science Bulletin*, vol. 54, no. 14, pp. 2410–2415, Jul. 2009.

[3] D. J. Müller and Y. F. Dufrêne, "Atomic force microscopy: a nanoscopic window on the cell surface," *Trends in Cell Biology*, vol. 21, no. 8, pp. 461–469, 2011.

[4] Y. K. Yong, A. Bazaei, S. O. R. Moheimani, and F. Allgöwer, "Design and Control of a Novel Non-Raster Scan Pattern for Fast Scanning Probe Microscopy," in *IEEE/ASME International Conference on Advanced Intelligent Mechatronics (AIM)*, Kachsiung, Taiwan, Jul., 11 – 14, 2012, pp. 456–461.

[5] G. Agarwal and T. M. Nocera, *The Nanobiotechnology Handbook*. CRC Press, 2012, ch. Atomic Force Microscopy, pp. 369–392.

[6] G. Schitter and M. J. Rost, "Scanning probe microscopy at video-rate," *Materials Today*, vol. 11, no. 0, pp. 40–48, 2008.

[7] B. Song, N. Xi, R. Yang, K. W. C. Lai, and C. Qu, "Video Rate Atomic Force Microscopy (AFM) Imaging using Compressive Sensing," in *11th IEEE International Conference on Nanotechnology*, Portland, Oregon, USA, Aug. 15-18, 2011, pp. 1056–1059.

[8] Y. K. Yong, S. O. R. Moheimani, and I. R. Petersen, "High-speed cycloid-scan atomic force microscopy," *Nanotechnology*, vol. 21, no. 36, p. 4, Aug. 2010.

[9] T. Tuma, J. Lygeros, V. Kartik, A. Sebastian, and A. Pantazi, "High-speed multiresolution scanning probe microscopy based on Lissajous scan trajectories," *Nanotechnology*, vol. 23, no. 18, p. 9, Apr. 2012.

[10] T. Tuma, A. Sebastian, J. Lygeros, and A. Pantazi, "The four pillars of nanopositioning for scanning probe microscopy: The position sensor, the scanning device, the feedback controller, and the reference trajectory," *IEEE Control Systems*, vol. 33, no. 6, pp. 68–85, Dec. 2013.

[11] B. Bhushan and O. Marti, "Scanning Probe Microscopy – Principle of Operation, Instrumentation, and Probes," in *Springer Handbook of Nanotechnology*, B. Bhushan, Ed. Springer Berlin Heidelberg, 2010, ch. 21, pp. 573–617.

[12] D. Y. Abramovitch, S. B. Andersson, L. Y. Pao, and G. Schitter, "A Tutorial on the Mechanisms, Dynamics, and Control of Atomic Force Microscopes," in *American Control Conference*, New York City, USA, Jul. 11-13, 2007, pp. 3488–3502.

[13] T. Tuma, J. Lygeros, A. Sebastian, and A. Pantazi, "Optimal scan trajectories for high-speed scanning probe microscopy," in *American Control Conference (ACC)*, Montréal, Canada, Jun. 27 – 29, 2012, pp. 3791–3796.

[14] I. A. Mahmood, S. O. R. Moheimani, and B. Bhikkaji, "A New Scanning Method for Fast Atomic Force Microscopy," *IEEE Transactions on Nanotechnology*, vol. 10, no. 2, pp. 203–216, Mar. 2011.

[15] T. Ando, N. Kodera, E. T. A. Maruyama, K. Saito, and A. Toda, "A high-speed atomic force microscope for studying biological macromolecules," *Proceedings of the National Academy of Sciences of the United States of America*, vol. 98, no. 22, p. 12468–12472, Oct. 2001.

[16] S. B. Andersson and L. Y. Pao, "Non-Raster Sampling in Atomic Force Microscopy: A Compressed Sensing Approach," in *American Control Conference (ACC)*, Montréal, Canada, Jun. 27-29, 2012, pp. 2485–2490.

[17] T. R. Meyer, D. Ziegler, C. Brune, A. Chen, R. Farnham, N. Huynh, J.-M. Chang, A. L. Bertozzi, and P. D. Ashby, "Height drift correction in non-raster atomic force microscopy," *Ultramicroscopy*, vol. 137, pp. 48–54, Feb 2014.

[18] A. Chen, A. L. Bertozzi, P. D. Ashby, P. Getreuer, and Y. Lou, "Enhancement and Recovery in Atomic Force Microscopy Images," in *Excursions in Harmonic Analysis*, ser. Applied and Numerical Harmonic Analysis,, T. D. Andrews, R. Balan, J. J. Benedetto, W. Czaja, and K. A. Okoudjou, Eds. Birkhäuser Boston, 2013, vol. 2, pp. 311–332.

[19] A. Labuda, M. Lysy, W. Paul, Y. Miyahara, P. Grütter, R. Bennewitz, and M. Sutton, "Stochastic noise in atomic force microscopy," *Phys. Rev. E*, vol. 86, p. 031104, Sep. 2012.

[20] J. F. Claerbout and F. Muir, "Robust modeling with erratic data," *Geophysics*, vol. 38, no. 5, pp. 826–844, 1973.

[21] S. Levy and P. K. Fullagar, "Reconstruction of a sparse spike train from a portion of its spectrum and application to high-resolution deconvolution," *Geophysics*, vol. 46, no. 9, pp. 1235–1243, 1981.

[22] F. Santosa and W. W. Symes, "Linear inversion of band-limited reflection seismograms," *SIAM Journal on Scientific and Statistical Computing*, vol. 7, no. 4, pp. 1307–1330, 1986.

[23] E. J. Candès, J. Romberg, and T. Tao, "Robust Uncertainty Principles: Exact Signal Reconstruction From Highly Incomplete Frequency Information," *IEEE Transactions on Information Theory*, vol. 52, no. 2, pp. 489–509, Feb. 2006.

[24] D. L. Donoho, "Compressed Sensing," *IEEE Transactions on Information Theory*, vol. 52, no. 4, pp. 1289–1306, Apr. 2006.

[25] R. G. Baraniuk, "Compressive sensing [lecture notes]," *IEEE Signal Processing Magazine*, vol. 24, no. 4, pp. 118–121, Jul. 2007.

[26] E. J. Candès and M. B. Wakin, "An Introduction To Compressive Sampling," *IEEE Signal Processing Magazine*, vol. 25, no. 2, pp. 21–30, Mar. 2008.

[27] J. Romberg, "Imaging via Compressive Sampling," *IEEE Signal Processing Magazine*, vol. 25, no. 2, pp. 14–20, Mar. 2008.

[28] E. J. Candès, "The restricted isometry property and its implications for compressed sensing," *Comptes Rendus Mathematique*, vol. 346, no. 9–10, pp. 589–592, 2008.

[29] S. Nam, M. Davies, M. Elad, and R. Gribonval, "The cosparse analysis model and algorithms," *Applied and Computational Harmonic Analysis*, vol. 34, no. 1, pp. 30–56, 2013.

[30] D. L. Donoho and J. Tanner, "Precise Undersampling Theorems," *Proceedings of the IEEE*, vol. 98, no. 6, pp. 913–924, Jun. 2010.

[31] T. L. Jensen, T. Arildsen, J. Østergaard, and T. Larsen, "Reconstruction of Undersampled Atomic Force Microscopy Images : Interpolation versus Basis Pursuit," in *International Conference on Signal-Image Technology&Internet-Based Systems (SITIS)*, Kyoto,Japan, Dec. 2 – 5, 2013, p. 6.

[32] G. Strang, *Introduction to Linear Algebra*, 2nd ed. Wellesley-Cambridge Press, 1998.

[33] E. J. Candès, Y. C. Eldar, D. Needell, and P. Randall, "Compressed sensing with coherent and redundant dictionaries," *Applied and Computational Harmonic Analysis*, vol. 31, no. 1, pp. 59–73, 2011.

[34] R. Rubinstein, A. M. Bruckstein, and M. Elad, "Dictionaries for Sparse Representation Modeling," *Proceedings of the IEEE*, vol. 98, no. 6, pp. 1045–1057, Jun. 2010.

[35] S. G. Mallat and Z. Zhang, "Matching Pursuits With Time-Frequency Dictionaries," *IEEE Transactions on Signal Processing*, vol. 41, no. 12, pp. 3397–3415, Dec. 1993.

[36] S. S. Chen, D. L. Donoho, and M. A. Saunders, "Atomic Decomposition by Basis Pursuit," *Siam Review*, vol. 43, no. 1, pp. 129–159, Mar. 2001.

[37] W. D. Ray and R. M. Driver, "Further Decomposition of the Karhunen-Loève Representation of a Stationary Random Process," *IEEE Transactions on Information Theory*, vol. IT-16, no. 6, pp. 663–668, Nov. 1970.

[38] R. O. Duda, P. E. Hart, and D. G. Stork, *Pattern Classification*, 2nd ed. Wiley-Blackwell, 2000.

[39] B. A. Olshausen and D. J. Field, "Sparse Coding with an Overcomplete Basis Set: A Strategy Employed by V1?" *Vision Research*, vol. 37, no. 23, pp. 3311–3325, Dec. 1997.

[40] M. Aharon, M. Elad, and A. Bruckstein, "K-SVD: An Algorithm for Designing Overcomplete Dictionaries for Sparse Representation," *Signal Processing, IEEE Transactions on*, vol. 54, no. 11, pp. 4311–4322, Nov. 2006.

[41] G. Strang and T. Nguyen, *Wavelets and Filter Banks*. Wellesley, USA: Wellesley-Cambridge Press, 1996.

[42] G. K. Wallace, "The JPEG Picture Compression Standard," *IEEE Transactions on Consumer Electronics*, vol. 38, no. 1, pp. 18–34, Feb. 1992.

[43] H. S. Anderson, J. Ilic-Helms, B. Rohrer, J. Wheeler, and K. Larson, "Sparse imaging for fast electron microscopy," in *Computational Imaging XI, Proceedings of the SPIE*, vol. 8657, Burlingame, California, USA, Feb. 3 2013, pp. (86 570C–1)–(86 570C–12).

[44] A. Skodras, C. Christopoulos, and T. Ebrahimi, "The JPEG 2000 Still Image Compression Standard," *IEEE Signal Processing Magazine*, vol. 18, no. 5, pp. 36–58, Sep. 2001.

[45] L. He and L. Carin, "Exploiting Structure in Wavelet-Based Bayesian Compressive Sensing," *IEEE Transactions on Signal Processing*, vol. 57, no. 9, pp. 3488–3497, Sep. 2009.

[46] S. Som and P. Schniter, "Compressive Imaging Using Approximate Message Passing and a Markov-Tree Prior," *IEEE Transactions on Signal Processing*, vol. 60, no. 7, pp. 3439–3448, Jul. 2012.

[47] M. Afonso, J. Bioucas-Dias, and M. Figueiredo, "Fast image recovery using variable splitting and constrained optimization," *IEEE Transactions on Image Processing*, vol. 19, no. 9, pp. 2345–2356, Sep. 2010.

[48] R. Tibshirani, "Regression shrinkage and selection via the lasso," *Journal of the Royal Statistical Society. Series B (Methodological)*, vol. 58, no. 1, pp. 267–288, 1996.

[49] S. S. Chen, D. L. Donoho, and M. A. Saunders, "Atomic decomposition by basis pursuit," *SIAM Journal on Scientific Computing*, vol. 20, no. 1, pp. 33–61, 1998.

[50] S. Boyd and L. Vandenberghe, *Convex Optimization*. Cambridge: Cambridge University Press, 2004.

[51] D. Bertsekas, *Convex Optimization Algorithms*. Athena Scientific, 2015.

[52] P. Combettes and J.-C. Pesquet, "Proximal splitting methods in signal processing," in *Fixed-Point Algorithms for Inverse Problems in Science and Engineering*, ser. Springer Optimization and Its Applications, H. H. Bauschke, R. S. Burachik, P. L. Combettes, V. Elser, D. R. Luke, and H. Wolkowicz, Eds. Springer New York, 2011, pp. 185–212.

[53] E. van den Berg and M. P. Friedlander, "Probing the Pareto frontier for basis pursuit solutions," *SIAM Journal on Scientific Computing*, vol. 31, no. 2, pp. 890–912, 2008.

[54] J. Yang and Y. Zhang, "Alternating direction algorithms for ℓ_1-problems in compressive sensing," *SIAM Journal on Scientific Computing*, vol. 33, no. 1, pp. 250–278, 2011.

[55] J. Dahl, P. C. Hansen, S. H. Jensen, and T. L. Jensen, "Algorithms and software for total variation image reconstruction via first-order methods," *Numerical Algorithms*, vol. 53, no. 1, pp. 67–92, 2010.

[56] L. I. Rudin, S. Osher, and E. Fatemi, "Nonlinear total variation based noise removal algorithms," *Physica D: Nonlinear Phenomena*, vol. 60, no. 1–4, pp. 259–268, 1992.

[57] D. Needell and R. Ward, "Stable Image Reconstruction Using Total Variation Minimization," *SIAM Journal on Imaging Sciences*, vol. 6, no. 2, pp. 1035–1058, 2013.

[58] D. Ziegler, T. R. Meyer, R. Farnham, C. Brune, A. L. Bertozzi, and P. D. Ashby, "Improved accuracy and speed in scanning probe microscopy by image reconstruction from non-gridded position sensor data," *Nanotechnology*, vol. 24, no. 33, p. 335703, 2013.

[59] P. Combettes and J. Pesquet, "Image restoration subject to a total variation constraint," *IEEE Transactions on Image Processing*, vol. 13, no. 9, pp. 1213–1222, Sep. 2004.

[60] T. Goldstein and S. Osher, "The Split Bregman Method for L1-Regularized Problems," *SIAM Journal on Imaging Sciences*, vol. 2, no. 2, pp. 323–343, 2009.

[61] P. Combettes and J. Pesquet, "A douglas-rachford splitting approach to nonsmooth convex variational signal recovery," *IEEE Journal of Selected Topics in Signal Processing*, vol. 1, no. 4, pp. 564–574, Dec. 2007.

[62] A. Beck and M. Teboulle, "Fast gradient-based algorithms for constrained total variation image denoising and deblurring problems," *IEEE Transactions on Image Processing*, vol. 18, no. 11, pp. 2419–2434, Nov. 2009.

[63] S. Becker, E. J. Candès, and M. C. Grant, "Templates for convex cone problems with applications to sparse signal recovery," *Mathematical Programming Computation*, vol. 3, no. 3, pp. 165–218, 2011.

[64] T. Blumensath, M. E. Davies, and G. Rilling, "Greedy algorithms for compressed sensing," in *Compressed Sensing: Theory and Applications*, Y. C. Eldar and G. Kutyniok, Eds. Cambridge University Press, 2012, ch. 8, pp. 348–393.

[65] Y. C. Pati, R. Rezaiifar, and P. S. Krishnaprasad, "Orthogonal Matching Pursuit: Recursive Function Approximation with Applications to Wavelet Decomposition," in *Twenty-Seventh Asilomar Conference on Signals,Systems and Computers*, vol. 1, Pacific Grove,California,USA, Nov. 1 – 3, 1993, pp. 40–44.

[66] T. Blumensath and M. E. Davies, "Iterative Thresholding for Sparse Approximations," *Journal of Fourier Analysis and Applications*, vol. 14, no. 5-6, pp. 629–654, Sep. 2008.

[67] I. Daubechies, M. Defrise, and C. D. Mol, "An Iterative Thresholding Algorithm for Linear Inverse Problems with a Sparsity Constraint," *Communications on Pure and Applied Mathematics*, vol. 57, no. 11, pp. 1413–1457, Nov. 2004.

[68] W. Dai and O. Milenkovic, "Subspace Pursuit for Compressive Sensing Signal Reconstruction," *IEEE Transactions on Information Theory*, vol. 55, no. 5, pp. 2230–2249, May 2009.

[69] D. Needell and J. A. Tropp, "CoSaMP: Iterative signal recovery from incomplete and inaccurate samples," *Applied and Computational Harmonic Analysis*, vol. 26, no. 3, p. 301–321, May 2009.

[70] A. Maleki and D. L. Donoho, "Optimally Tuned Iterative Reconstruction Algorithms for Compressed Sensing," *IEEE Journal Selected Topics in Signal Processing*, vol. 4, no. 2, pp. 330–341, Apr. 2010.

[71] J. D. Blanchard and J. Tanner, "Performance comparisons of greedy algorithms in compressed sensing," *Numerical Linear Algebra with Applications*, 2014.

[72] A. Maleki and A. Montanari, "Analysis of Approximate Message Passing Algorithm," in *44th Annual Conference on Information Sciences and Systems (CISS)*, Princeton, New York, USA, Mar. 17–19, 2010.

[73] J. Vila and P. Schniter, "Expectation-Maximization Gaussian-Mixture Approximate Message Passing," in *46th Annual Conference on Information Sciences and Systems (CISS)*, Princeton, New Jersey, USA, Mar. 21 – 23, 2012, p. 6.

[74] S. Rangan, P. Schniter, and A. Fletcher, "On the convergence of approximate message passing with arbitrary matrices," in *Information Theory (ISIT), 2014 IEEE International Symposium on*, June 2014, pp. 236–240.

[75] D. L. Donoho, A. Maleki, and A. Montanari, "Message-passing algorithms for compressed sensing," *Proceedings of the National Academy of Sciences of the United States of America*, vol. 106, no. 45, p. 18914–18919, Nov. 2009.

[76] ——, "Message Passing Algorithms for Compressed Sensing: I. Motivation and Construction," in *IEEE Information Theory Workshop (ITW)*, Cairo, Egypt, Jan. 6 – 8, 2010, p. 5.

[77] ——, "Message Passing Algorithms for Compressed Sensing: II. Analysis and Validation," in *IEEE Information Theory Workshop (ITW)*, Cairo, Egypt, Jan. 6 – 8, 2010, p. 5.

[78] S. Rangan, "Generalized Approximate Message Passing for Estimation with Random Linear Mixing," in *IEEE International Symposium on Information Theory (ISIT)*, St. Petersburg, Russia, Jul. 31 – Aug. 5, 2011, pp. 2168–2172.

[79] J. P. Vila and P. Schniter, "Expectation-Maximization Gaussian-Mixture Approximate Message Passing," *IEEE Transactions on Signal Processing*, vol. 61, no. 19, pp. 4658–4672, Oct. 2013.

[80] A. Maleki and R. Baraniuk, "Least Favorable Compressed Sensing Problems for First-Order Methods," in *IEEE International Symposium on Information Theory (ISIT)*, St. Petersburg, Russia, Jul. 31 – Aug. 5, 2011, pp. 134–138.

[81] V. Smidl and A. Quinn, *The Variational Bayes Method in Signal Processing*. Springer, 2006.

[82] M. Lighthill, *An Introduction to Fourier Analysis and Generalised Functions*. Cambridge University Press, 1958.

[83] S. S. Goha and I. G. H. Ong, "Reconstruction of bandlimited signals from irregular samples," *Signal Processing*, vol. 46, no. 3, pp. 315–329, 1995.

[84] L. P. Yaroslavsky, G. Shabat, B. G. Salomon, I. A. Ideses, and B. Fishbain, "Nonuniform sampling, image recovery from sparse data and the discrete sampling theorem," *J. Opt. Soc. Am. A*, vol. 26, no. 3, pp. 566–575, Mar. 2009.

[85] M. de Berg, M. van Kreveld, M. Overmars, and O. Schwarzkopf, *Computational Geometry: Algorithms and Applications*. Springer Berlin Heidelberg, 1997.

[86] I. Clark, *Practical Geostatistics*. Alloa, Scotland: Geostokos Limited, 1979.

[87] S. Lee, G. Wolberg, and S. Y. Shin, "Scattered data interpolation with multilevel B-splines," *IEEE Transactions on Visualization and Computer Graphics*, vol. 3, no. 3, pp. 228–244, Jul. 1997.

[88] A. Aldroubi, "Non-uniform weighted average sampling and reconstruction in shift-invariant and wavelet spaces," *Applied and Computational Harmonic Analysis*, vol. 13, no. 2, pp. 151–161, 2002.

[89] Z. Wang, A. C. Bovik, H. R. Sheikh, and E. P. Simoncelli, "Image Quality Assessment: From Error Visibility to Structural Similarity," *IEEE Transactions on Image Processing*, vol. 13, no. 4, pp. 600–612, Apr. 2004.

[90] K. Moreland, "Diverging Color Maps for Scientific Visualization," in *Advances in Visual Computing: 5th International Symposium, ISVC*, G. Bebis, R. Boyle, B. Parvin, D. Koracin, Y. Kuno, J. Wang, R. Pajarola, P. Lindstrom, A. Hinkenjann, M. L. Encarnação, C. T. Silva, and D. Coming, Eds. Las Vegas, NV, USA,: Springer Berlin Heidelberg, Nov. 30 – Dec. 2 2009, vol. 5876, pp. 92–103, proceedings Part II.

[91] F. Pérez, B. E. Granger, and J. D. Hunter, "Python: An ecosystem for scientific computing," *Computing in Science & Engineering*, vol. 13, no. 2, pp. 13–21, Mar.–Apr. 2011.

[92] T. Oliphant, "Python for scientific computing," *Computing in Science & Engineering*, vol. 9, no. 3, pp. 10–20, 2007.

[93] P. Vandewalle, J. Kovačević, and M.Vetterli, "Reproducible research in signal processing [what, why, and how]," *IEEE Signal Processing Magazine*, pp. 37–47, May 2009.

[94] M. Schwab, M. Karrenbach, and J. Claerbout, "Making scientific computations reproducible," *Computing in Science & Engineering*, vol. 2, no. 6, pp. 61–67, 2000.

[95] C. S. Oxvig, P. S. Pedersen, T. Arildsen, J. Østergaard, and T. Larsen, "Magni: A Python Package for Compressive Sampling and Reconstruction of Atomic Force Microscopy Images," *Journal of Open Research Software*, vol. 2, no. 1, p. e29, Oct. 2014.

[96] E. Jones, T. Oliphant, P. Peterson *et al.*, "SciPy: Open source scientific tools for Python," 2001–, [Online; accessed 2015-02-25].

[97] R. G. Baraniuk, V. Cevher, M. F. Duarte, and C. Hegde, "Model-Based Compressive Sensing," *IEEE Transactions on Information Theory*, vol. 56, no. 4, pp. 1982–2001, Apr. 2010.

[98] M. F. Duarte and Y. C. Eldar, "Structured Compressed Sensing: From Theory to Applications," *IEEE Transactions on Signal Processing*, vol. 59, no. 9, pp. 4053–4085, Sep. 2011.

[99] J. Yang, Y. Zhang, and W. Yin, "A fast alternating direction method for tvl1-l2 signal reconstruction from partial fourier data," *IEEE Journal of Selected Topics in Signal Processing*, vol. 4, no. 2, pp. 288–297, Apr. 2010.

Christian Schou Oxvig (S'14) received the B.Sc. and M.Sc. degrees in electrical and computer engineering from Aalborg University in 2011 and 2013, respectively. He is currently a Ph.D. student in the Signal and Information Processing Section, Department of Electronic Systems, Aalborg University. His research interests include scientific computing, statistical signal processing, and reproducibility in computer and simulation experiments.

Patrick Steffen Pedersen (M'15) received the B.Sc. and M.Sc. degrees in electrical and computer engineering from Aalborg University in 2011 and 2013, respectively. He is currently pursuing the Ph.D. degree at the Signal and Information Processing Section of the Department of Electronic Systems at Aalborg University. His current research interests lie in the area of signal processing and compressed sensing.

Jan Østergaard (S'98–M'99–SM'11) received the M.Sc.E.E. from Aalborg University, Aalborg, Denmark, in 1999 and the PhD degree (cum laude) from Delft University of Technology, Delft, The Netherlands, in 2007. From 1999 to 2002, he worked as an R&D Engineer at ETI A/S, Aalborg, Denmark, and from 2002 to 2003, he worked as an R&D Engineer at ETI Inc., Virginia, United States. Between September 2007 and June 2008, he worked as a post-doctoral researcher at The University of Newcastle, NSW, Australia. From June 2008 to March 2011, he worked as a post-doctoral researcher/Assistant Professor at Aalborg University. Since 2011 he has been an Associate Professor at Aalborg University. He has been a visiting researcher at Tel Aviv University, Tel Aviv, Israel, and at Universidad Técnica Federico Santa María, Valparaíso, Chile. He has received a Danish Independent Research Council's Young Researcher's Award, a best PhD thesis award by the European Association for Signal Processing (EURASIP), and fellowships from the Danish Independent Research Council and the Villum Foundation's Young Investigator Programme. He is an Associate Editor of EURASIP Journal on Advances in Signal Processing.

Torben Larsen (S'88–M'99–SM'04) received the M.Sc.E.E. and Dr.Techn. degrees from Aalborg University, Aalborg, Denmark, in 1988 and 1998, respectively. Since 2001, he has been a Full Professor at Aalborg University in electronic circuits, signals and systems theory. He has industrial experience working as senior engineer at Bosch Telecom and Siemens Mobile Phones. He was member in 2005-2010 and vice-chairman in 2009-2010 of the Danish Research Council for Technology and Production Sciences. In 2011 he was appointed director of the doctoral school at The Faculty of Engineering and Science, Aalborg University, with more than 650 enrolled PhD students. He has authored or co-authored over 130 peer-reviewed journal and conference papers and contributed to four internationally published books. He received the Spar Nord Research Prize in 1999 and "Aalborg University Teacher of the year 2013". Since 2007 he has been member of the Academy of Technical Sciences, Denmark. He has supervised approx. 25 PhD students. He has been Vice Dean at the Faculty of Engineering and Science, Aalborg University since 2015. His recent research interests mainly include scientific computing, compressive sensing, numerical algorithms etc. in the areas of signals and systems theory.

Thomas Arildsen (S'03–M'04–S'06–M'10) received the M.Sc.E.E. and Ph.D. degrees from Aalborg University, Aalborg, Denmark, in 2004 and 2010, respectively. From 2004 to 2006, he worked as project engineer at RTX Telecom A/S in Aalborg, Denmark. He has been a visiting Ph.D. student at University of Miami, United States in 2007. He has worked at Aalborg University since 2010, as associate professor since 2014. His research interests include compressed sensing, image processing, analog-to-information conversion, scientific computing, statistical signal processing, estimation, communication signal processing.